

Sn AND Ti DIFFUSION, PHASE FORMATION, STOICHIOMETRY, AND
SUPERCONDUCTING PROPERTIES OF INTERNAL-Sn-TYPE Nb₃Sn
CONDUCTORS

A Thesis

Presented in Partial Fulfillment of the Requirements for
The Degree of Master of Science in the Graduate
School of the Ohio State University

By

Rakesh Kumar Dhaka, B. Tech.

The Ohio State University
2007

Masters Examination Committee

Professor Mike Sumption, Adviser

Professor John Morral, Adviser

Professor Katharine Flores

ABSTRACT

In the present work the diffusion of Sn through the interfilamentary matrix within a subelement and the formation of the associated Cu-Sn intermetallics were observed experimentally for several different Nb₃Sn internal-Sn type strands during the pre-reaction part of the heat treatment. An analytical-based model was then developed to determine the time and temperature dependence of Sn-diffusion through the Cu matrix of Nb₃Sn subelements. The output of the model is in the form of radial positions of η , ε and α phases as a function of time during pre-reaction heat treatment process. These predicted radial positions can be used to determine the optimum heat treatment parameters. The model was then compared to the experimental results. Experimental results for Ti-bearing superconductor strands were also discussed.

Following the pre-reaction heat treatment studies, the effects of Titanium doping in presence of Tantalum on the kinetics of Nb₃Sn formation and superconducting properties of internal-tin type strands were examined. A series of internal-tin type Nb₃Sn subelements which had Nb-7.5wt%Ta filaments and various levels of Ti doping were investigated. Titanium was introduced into the Sn core of the subelements such that the core contained 0 at% to 2.8 at% Ti before reaction. A series of pre-reaction and reaction heat treatments were then given to these strands. The Ti and Sn distributions were

mapped throughout the strand cross-sections for samples removed at various stages of the heat treatment. The formation rates of Nb_3Sn phases containing different levels of Ti were determined. Transport current, upper critical field, and the compositions of the A15 regions were measured for strands doped with various levels of Ti. The influence of simultaneous Ti and Ta doping on the upper critical field as well as high field J_c optimization was investigated and it was found that addition of Ti in presence of 7.5 wt% Ta in Nb filaments does not improve the B_{c2} .

ACKNOWLEDGMENTS

It is a great pleasure for me to thank many people who have helped me throughout my study, and research work at the Ohio State University. First of all, I express my deep sense of gratitude and sincere thanks to my advisor, Dr. Michael Sumption for his guidance, valuable suggestions and constant encouragement. I am obliged to him for giving me the opportunity to work at LASM (Laboratory for Applied Superconductivity and Magnetism).

I am also sincerely thankful to my advisor, Dr. John Morral for the many helpful discussions and guidance through out my research work. His wide knowledge of the subject and explanation style along with his cheerful personality has been a great value for me. I am also grateful to him for his help and suggestions regarding my future career.

I wish to express my sincere thanks to Dr. Edward W. Collings for his explanation of the things concisely and in a very simple way.

I would like to thank Eric Gregory (Supergenics LLC), Michael Tomsic (Hyperterch Research Inc.), and Xuan Peng (Global Research Inc.) for providing most of the superconducting samples for this work. I am grateful to Xuan Peng for sharing her knowledge on the subject and also for clearing my doubts related to the manufacturing process. I appreciate her help for the heat treatments and microscopy of some of my samples.

I am also thankful to the technical staff in the Materials Science and Engineering department at the Ohio State University especially Cameron Begg, Steve Bright and Henk Colijn for their assistance in operating the SEM, TEM, FIB and Optical microscopes.

I thank my fellow graduate students Mohit Bhatia, Scot Bohnenstiehl, Michael Susner and Vishal Nazareth for making my time at LASM enjoyable.

Lastly, I am grateful to my parents and family members for their love and constant support for all of my endeavors.

VITA

December 31, 1982. Born – Hanumangarh, India

2000-2004. B.Tech, Ceramic Engineering,
Institute of Technology, Banaras Hindu University, India

2004-2005. Development Engineer, R&D Division,
Larsen & Toubro Limited, India

2005-2007. Graduate Research Associate,
The Ohio State University, USA

FIELDS OF STUDY

Major Field: Materials Science and Engineering

TABLE OF CONTENTS

	Page
Abstract	ii
Acknowledgments	iv
Vita	vi
List of Tables	ix
List of Figures	x
Chapter 1 : INTRODUCTION AND REVIEW OF SUPERCONDUCTIVITY	1
1.1 Introduction.....	1
1.2 Superconductivity.....	3
Chapter 2 : Nb₃Sn SUPERCONDUCTORS	10
2.1 Introduction.....	10
2.2 Properties of Nb ₃ Sn.....	11
2.2.1 Crystal Structure	11
2.2.2 Nb-Sn Phase Diagram.....	12
2.2.3 Dependence of H_{c2} and T_c on Sn Composition.....	13
2.2.4 Titanium and Tantalum Additions to A15 Nb ₃ Sn.....	15
2.3 Manufacturing Methods.....	18
2.3.1 The Bronze Process.....	18
2.3.2 The Internal Tin Process.....	21
2.3.3 The Powder in Tube Process.....	23
Chapter 3 : SAMPLES PREPARATION	25
3.1 Sample Specifications.....	25
3.1.1 Samples for Cu-Sn Diffusion Study.....	25
3.1.2 Samples for Study of the Effect of Ti Addition.....	28
3.2 Heat Treatment.....	30
3.3. Sample Preparation for Electron Microscopy.....	32
Chapter 4 : EXPERIMENTAL METHODS	35
4.1 Introduction.....	35

4.2 SEM, EDS and Image Analysis.....	35
4.3 Critical Current Measurement.....	42
4.4 Upper Critical Field (B_{c2}) Measurement.....	43
Chapter 5 : MEASUREMENTS OF DIFFUSION AND PHASE FORMATION	45
5.1 Introduction.....	45
5.2 Intermetallic Formation.....	48
5.3 The Cu-Sn System.....	49
5.4 Growth Rates of Cu-Sn Intermetallics.....	49
5.5 Analytical Model.....	54
5.5.1 The Model.....	54
5.5.2 Experimental Verification.....	60
5.6 Growth Rates of Nb ₃ Sn Formation.....	61
Chapter 6 : EFFECTS OF Ti ADDITIONS ON THE SUPERCONDUCTING	
PROPERTIES.....	68
6.1 Introduction.....	68
6.2 Effect of Ti Addition on B_{c2} Values.....	69
6.3 Effect of Ti Addition on J_c Values.....	71
6.4 Discussion.....	72
Chapter 7 : CONCLUSION.....	76
List of References	78

LIST OF TABLES

Table	Page
2.1 Superconducting properties of the high field A15 compounds [23].....	10
3.1 Specifications of samples for Cu-Sn diffusion study.....	28
3.2 Specifications of samples for the study of effect of Ti addition.....	30
5.1 The pre-reaction heat treatment schedule for four different types of sublements EG23, EG24, GL28 and GL29.....	50
5.2 Growth rate parameters for η and ε phases at 400°C.....	54
5.3 Values of densities, growth rate parameters and weight fractions of Sn in η and ε phases.....	57
5.4 Heat treatment schedule for four different types of sublements G0, G2, G3 and G4	64
5.5 k and n for Nb ₃ Sn layer growth in the barrier of G0-G4 subelements.....	67
6.1 B_{c2} values (in Tesla) for the four strand types (G0, G2, G3, and G4) after heat treatment at three different temperatures (675°C, 700°C and 725°C) for heat treatment durations ranging from 100 hours to 225 hours. The optimum value of B_{c2} at each temperature for each of the strands is shown as bold.....	70
6.2 Comparison of J_c and B_{c2} values for the strands with their heat treatment optimized for B_{c2}	74

LIST OF FIGURES

Figure		Page
1.1	Illustration of the drop to zero resistivity in superconducting materials at a temperature T_c compared to non-superconducting materials.....	4
1.2	An illustration of the Meissner effect in a superconductor.....	5
1.3	H-T phase space diagram for Type I superconductors.....	7
1.4	H-T phase space diagram for Type II superconductors.....	8
1.5	Flux lines in type II superconductors and the forces acting on fluxons in a applied field B_a with current I passing through it. The Lorentz force on the fluxons (F_L) is opposed by the pinning force (F_P). When $F_L > F_P$, the fluxons move and energy dissipation occurs.....	9
2.1	The A15 crystal structure of Nb_3Sn . Sn atoms (light spheres) forming a <i>bcc</i> structure and two Nb atoms (dark spheres) forming mutually orthogonal chains across the faces (reprinted from [25]).....	11
2.2	The Nb-Sn phase diagram (after Charlesworth [27]).....	13
2.3	The critical temperature and critical field (at zero temperature) dependence on Sn composition. The solid curves represent best fit for the Data (reproduced from the work of Arno Godeke [25]).....	14
2.4	Schematic of cross section of the wire made by the bronze method.....	19
2.5	The Cu-Sn system (reproduced from [46]).....	20

2.6	Cross section of a wire made by the Internal-Tin process.....	21
2.7	The Modified Jelly Roll process.....	22
2.8	Cross section of the wire made by the Powder in Tube process.....	23
3.1	SEM-BSE images of sample EG23 (a) the cross-section of the sample, wire diameter 0.25 mm (b) Higher magnification of the filaments and the barrier; both are made of Nb 7.5 wt% Ta.....	26
3.2	SEM-BSE images of sample EG24 (a) the cross-section of the sample, wire diameter 0.25 mm (b) Higher magnification of the filaments and the barrier both having composition of Nb7.5wt%Ta, additionally all the filaments were wrapped with Nb47%Ti sheath.....	26
3.3	SEM-BSE images of sample GL28 (a) the cross-section of the sample, wire diameter 0.25 mm (b) Higher magnification of the filaments and the barrier. Filaments and barrier are made of pure Nb except the few filaments as seen in the image with slightly grey contrast are made of Nb47%Ti.....	27
3.4	SEM-BSE images of sample GL28 (a) the cross-section of the sample, wire diameter 0.25 mm (b) Higher magnification of the filaments and the barrier. Filaments and barrier are made of Nb7.5wt%Ta, except the few filaments as seen in the image with slightly grey contrast are made of Nb47%Ti.....	27
3.5	Internal-tin type subelements (a) sample G0 with pure Sn core (b) sample G2 with 1.4 at% Ti in core.....	29
3.6	Internal-tin type subelements (a) sample G3 with 2.1 at% Ti in the core (b) sample G4 with 2.8 at% Ti in the core.....	29

3.7	Typical heat treatment for the internal-tin type strands.....	32
3.8	Samples mounted for SEM (a) Hot mounted sample (b) Cold mounted sample.....	33
4.1	Products of the interaction of the electron beam and the specimen and the depth of information in scanning electron microscope. (The fluorescence emissions can come from as deep as 100 μm) (reprinted from [24]).....	36
4.2	Showing the shape and size of the specimen-beam interaction volume in a specimen of iron with an electron beam at 10-,20-, and 30-kV accelerating voltages.....	37
4.3	Shape and size of the specimen-beam interaction volume in specimens of different atomic number. Accelerating voltage is 20 kV.....	38
4.4	Monte-Carlo simulation showing the interaction volume for the Nb_3Sn specimen with accelerating voltage of 15 kV.....	39
4.5	(a) The SEM-BSE images of the superconducting subelement, (b) The converted binary image of the subelement (c,d,e) separated sections of the Sn core, Cu and the barrier respectively.....	41
4.6	(a) Short sample (2.5 cm long, diameter 0.25 mm) mounted on Cu plate (b) The Cu plate attached to the short sample measurement probe.....	43
4.7	A typical resistivity vs magnetic field curve for Nb_3Sn superconductors.....	44
5.1	The Cu-Sn system (reproduced from [46]).....	49

5.2	BSE-SEM examination of the growth of the ε and η phases in EG23 during the first step of the heat treatment at: (a) and (b) 210°C after 24 hrs; (c) and (d) 210°C after 48 hrs.....	51
5.3	BSE-SEM showing the growth of the ε and η phases in EG23 during the second step of the heat treatment for (a) and (b) 24 hrs at 400°C; (c) and (d) 48 hrs at 400°C.....	52
5.4	Growth of η and ε phases during pre-reaction heat treatment at 400°C for each type of strand. (Solid symbols: ε phase, Open symbol: η phase). η phase layer growth is shown before the depletion of Sn occurs. η phase growth data for GL29 has not been included here as the Sn depletion in this strand occurs just after 12 hrs at 400°C.....	53
5.5	Schematic of strand geometry showing the radial growth of η and ε phases after some time t during pre-reaction heat treatment.....	55
5.6	Radial positions within the subelement of η (\circ) and ε (\blacktriangledown) and pure Sn (\bullet) phase for EG23 during pre-reaction heat treatment. Calculated curves for R_η (---), R_ε (— —) and R_{Sn} (——) also shown. Horizontal dash-dot lines show inner boundaries of successive filamentary rows, six rows total. All radii normalized to R_{sub}	61
5.7	Radial positions within the subelement of η (\circ) and ε (\blacktriangledown) and pure Sn (\bullet) phase for EG24 during pre-reaction heat treatment. Calculated curves for R_η (---), R_ε (— —) and R_{Sn} (——) also shown. Horizontal dash-dot lines show inner boundaries of successive filamentary rows, six rows total. All radii normalized to R_{sub}	62
5.8	Radial positions within the subelement of η (\circ) and ε (\blacktriangledown) and pure Sn (\bullet) phase for GL28 during pre-reaction heat treatment. Calculated curves for R_η (---), R_ε (— —) and R_{Sn} (——) also shown. Horizontal dash-dot lines show inner boundaries of successive filamentary rows, six rows total. All	

	radii normalized to R_{sub}	63
5.9	Cross-sections of subelement G2 after heat treatments at 675°C for various times; (a) and (b) show that the Nb filaments and the Nb barrier are not fully converted into Nb ₃ Sn phase; (c) and (d) show that all the Nb filaments are converted into Nb ₃ Sn while the some portion of the Nb barrier is still unreacted; (e) and (f) Both the filaments and the barrier are converted to Nb ₃ Sn phase. In (f) the Sn has leaked into the outer Cu-matrix as the heat treatment time was too long (i.e. 225 h).....	65
5.10	Nb ₃ Sn layer growth in the barrier of each subelement type as a function of heat treatment time at three different temperature levels (675°C, 700°C, and 725°C).	66
6.1	Maximum B_{c2} as a function of temperature for all the four strand types. The maximum B_{c2} (resistive measurement) was selected (shown as bold text in Table 6.1) from the five different heat treatment durations (100 h, 150 h, 200 h, 200 h, and 225 h).....	71
6.2	Non-Cu J_c values of the strands having the optimum critical field (B_{c2}) for each strand type.....	72
6.3	Kramer plots for the strands with maximum B_{c2} . Values determined from the plot are shown in the legend. Kramer plot was fit to 16-23 T data only.....	74
6.4	Sn composition in the reacted A15 region for the strand which have maximum B_{c2} value (for each strand type). The EDS spot was at the center of the filaments.....	75

CHAPTER 1

INTRODUCTION AND REVIEW OF SUPERCONDUCTIVITY

1.1 Introduction

The development of Nb₃Sn superconductor has been continuous over the past few decades. One of the driving forces for this has been the increased demand for high field magnets. The upper critical field H_{c2} (the magnetic field where the transition from superconducting to normal state occurs) of Nb₃Sn has reached 28 T at 4.2 K [1]. And for high quality Nb₃Sn strands, the non-Cu critical current density, J_c , has reached beyond 3000 A/mm² at 12 T, 4.2 K [2].

Numerous studies have been carried out to find ways to improve the superconducting properties of Nb₃Sn. The main issues include increasing Sn content in Nb₃Sn system to achieve a more stoichiometric Nb₃Sn A15 phase, as well as decreasing the grain size for improved grain boundary pinning, resulting in improved critical current density J_c . Also, various elements have been added into Nb₃Sn strands to improve its superconducting properties and enhance Nb₃Sn formation.

Two kinds of elemental additions have investigated in the past. The first kind is non-transition elements, including Al [3], Ga [4], In [5], Sn [6], Ge [7], Mg [8] and Zn

[9]. Incorporation of non transition elements was found to be difficult except for Ga. On the other hand small additions of Mg accelerated Nb₃Sn formation. Since non-transition elements seldom improve superconducting properties and in most cases, decrease J_c , recent studies are mainly focused on another kind of addition including transition elements Zr [10], Hf [4], Ti [11-14] and Ta [15, 16]. These elements have d-bands similar to Nb. It is believed that these elements are substitution elements for the Nb sites in the A15 Nb₃Sn crystal structure, although their exact locations are unknown [17]. Both Zr and Hf were reported to accelerate Nb₃Sn layer growth. Whereas Ti and Ta addition accelerated the Nb₃Sn layer growth as well as enhanced the upper critical field H_{c2} . It has been known that both Ti and Ta act as impurities and increase normal state resistivity of Nb₃Sn, therefore, enhance H_{c2} [11-18].

In the present work, the two issues are investigated further to improve the properties of Nb₃Sn superconductors. First, is the diffusion of Sn during pre-reaction heat treatment and second the effects of Ti additions in presence of Ta on the properties of internal-tin type Nb₃Sn superconductors.

To investigate the diffusion of Sn and formation of the associated Cu-Sn intermetallics, four different types of Nb₃Sn strands were heat treated at 210°C and 400°C for various heat treatment durations. The growth of Cu-Sn intermetallics was measured and the growth rate constants were extracted. An analytical-based model was then developed to determine the time and temperature dependence of Sn-diffusion through the Cu matrix of Nb₃Sn strands. The output of the model is in the form of radial positions of η , ε and α phases as a function of time during pre-reaction heat treatment process. These

predicted radial positions were found to be in good agreement with the experimental results.

Following the Sn-diffusion study, the effects of Titanium doping in presence of Tantalum on the kinetics of Nb₃Sn formation and superconducting properties of internal-tin type strands were investigated. Four different types of internal-tin type Nb₃Sn strands which had Nb-7.5wt% Ta filaments and various levels of Ti doping (0 at to 2.8 at% in the core) were heat treated at three temperatures (675°C, 700°C and 725°C) for various heat treatment durations. The Ti and Sn distributions were mapped throughout the strand cross-sections for samples removed at various stages of the heat treatment. The formation rates of Nb₃Sn phases containing different levels of Ti were determined. Transport current, upper critical field, and the compositions of the A15 regions were measured for strands doped with various levels of Ti. The influence of simultaneous Ti and Ta doping on the upper critical field as well as high field J_c optimization was investigated. The additions of Ti in presence of Ta (7.5 wt% in Nb) have not improved the B_{c2} , although excellent subelement properties were seen.

1.2 Superconductivity

Many metals, alloys, and intermetallic compounds go through a phase transition at a *critical temperature*, T_c , to a state having zero electrical resistance (Figure 1.1); this phenomenon is one of the hallmark of *superconductivity* (discovered in 1911 by H. Kamerlingh Onnes[19]).

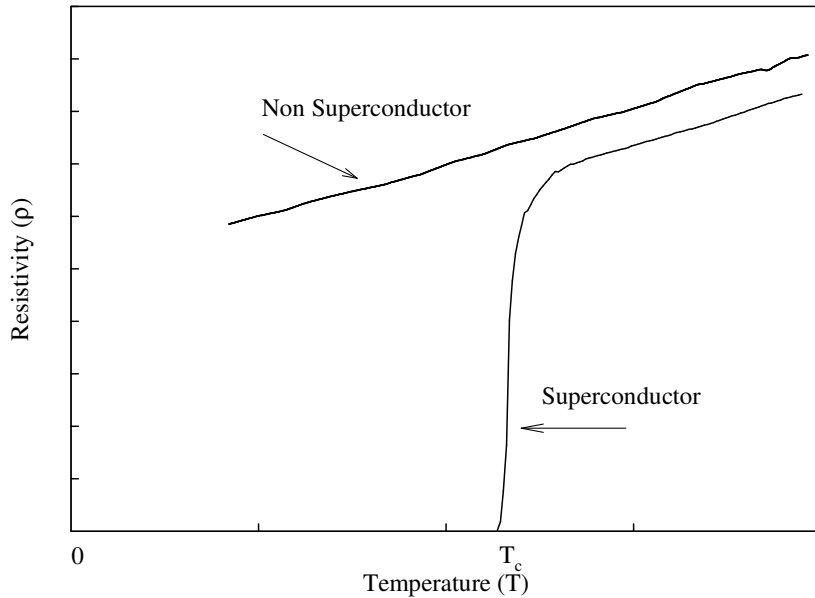


Figure 1.1 Illustration of the drop to zero resistivity in superconducting materials at a temperature T_c compared to non-superconducting materials.

In addition to the zero electrical resistance, a second hallmark of superconductivity is *Meissner effect* (Meissner and Ochsenfeld [20]). This refers to the expulsion of magnetic field from a superconductor below T_c , whether the sample is cooled in the field, or the field is applied after cooling (Figure 1.2). According to the constitutive equation for a magnetic material:

$$B = \mu_o (H + M) \quad (1.1)$$

Here $B(T)$ is the magnetic field induction within the sample, M (A/m) is the magnetization due to applied magnetic field H (A/m) and μ_o is permeability of free space which is equal to $4\pi \times 10^{-7}$ Wb/Am. For a Type I superconductor $B = 0$, which implies M

$= -H$. Therefore, the susceptibility, χ , defined as the ratio of the change in magnetization to the change in applied field, takes on the ideal value (-1) in the Meissner state:

$$\chi = \frac{dM}{dH} = -1 \quad (1.2)$$

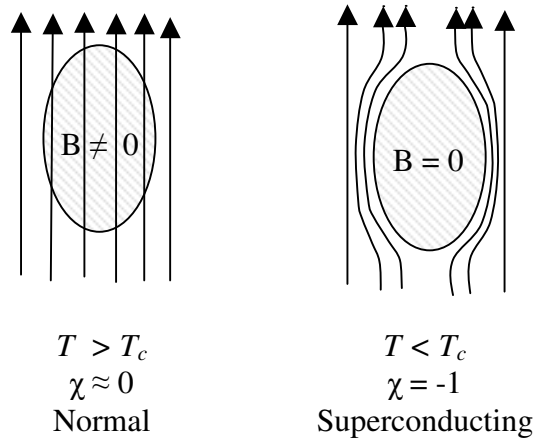


Figure 1.2 An illustration of the Meissner effect in a superconductor.

The superconductor remains in Meissner state i.e. $\chi = -1$ up to some *critical magnetic field*, H_c , whereupon it reverts to the normal state. H_c is temperature dependent.

In the Meissner state the magnetic field is excluded by developing shielding currents in the superconductor surface. The currents flow in a direction such that an opposing magnetic field is created inside the superconductor which cancels the applied field. The shielding currents are not confined to the surface of superconductor and flow to a finite depth on surface, called as penetration depth, λ , typically on the order of 100 nm.

Another important parameter for description of the superconductivity is the *coherence length*, ξ , which is defined as the distance over which an appreciable change in the density of the superconducting electrons can occur. In microscopic theory of Bardeen, Cooper and Schrieffer [21] this is identified as being the spatial extent of the Cooper pairs of electrons. The coherence length and the penetration depth are materials parameters.

In stoichiometric Nb₃Sn superconductor ξ and λ are about 3 nm and 60 nm respectively [22].

The relative values of ξ and λ determine the sign (positive or negative) of surface energy E_s at the interface between superconducting and normal region. The surface energy per unit area of the boundary is approximately expressed as:

$$E_s \approx \frac{1}{2} \mu_o H_c^2 (\xi - \lambda) \quad (1.3)$$

It can be seen from this expression that if coherence length is larger than the penetration depth, the interfacial energy becomes positive. This makes the transition from the superconducting to the normal state energetically favorable at H_c . Hence, first order transition to normal state occurs at H_c . The superconductors for which this takes place are called *Type I* superconductors. Most of the pure metals are Type I superconductors.

Alternatively, if the coherence length is smaller than the penetration depth, the interfacial energy becomes negative resulting in the penetration of the magnetic field in the superconductor above a lower critical field H_{c1} . At this point the magnetic flux penetrates in the form of discrete quanta called *fluxons*, and continues (by changing the

spacing between fluxons) up to an upper critical field H_{c2} (where the fluxons coalesce and superconductivity is quenched). These type of superconductors are called *Type II superconductors*. Most of the superconducting alloys, intermetallic compounds and oxides fall in this category. Schematic diagrams of Field-Temperature phase space for Type I and Type II superconductors are shown in Figure 1.3 and 1.4 respectively.

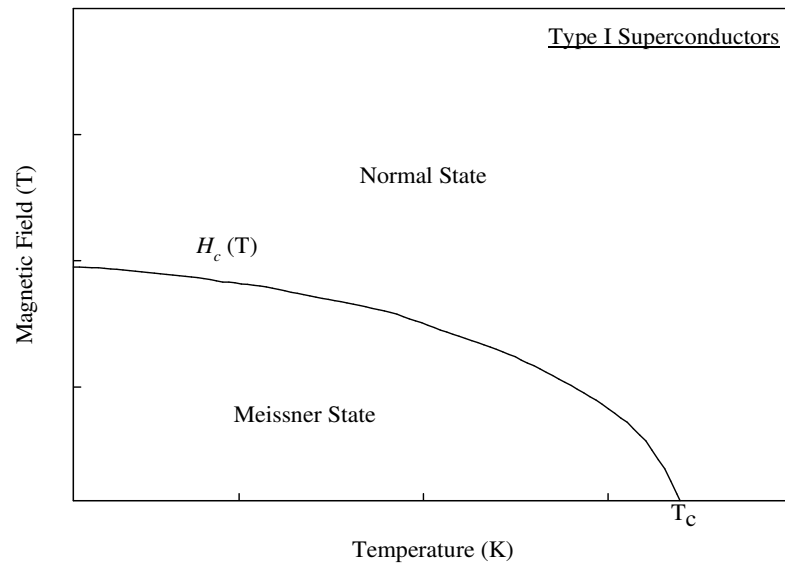


Figure 1.3 H-T phase space diagram for Type I superconductors.

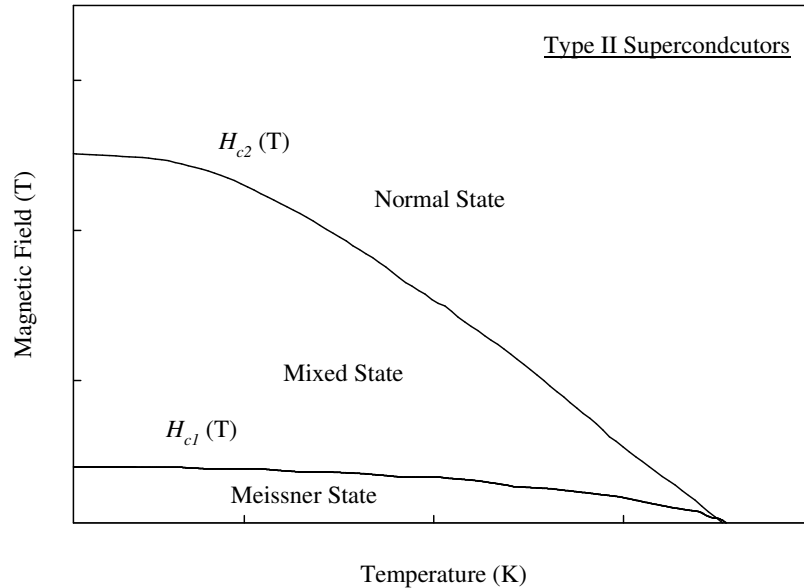


Figure 1.4 H-T phase space diagram for Type II superconductors.

In type II superconductors, when a current flows, a Lorentz force, F_L , acts on the fluxons. This force is perpendicular both to the field and the current direction causing the fluxons to move (Figure 1.5). This movement of fluxons results in the dissipation of energy. Hence, in order to have loss free current transport, the fluxons should be held stationary, or “pinned”. Imperfections in the materials (i.e. grain boundaries, solute atoms etc.) act as pinning centers and hinder fluxons motion with a flux pinning force F_p . The Lorentz force increases with the increase in current at a particular field and at some point the Lorentz force becomes equal to the pinning force allowing the fluxons to move. The current at which this happens is called *critical current*, I_c . A current higher than I_c results in motion of the fluxons, generating energy loss and a voltage across the

conductor. On the other hand, the magnetic field at which the pinning force becomes zero (leading to zero critical current) is called the irreversibility field, H^* . This tends to be close in value to H_{c2} but not necessarily equal. Hence, at a magnetic field below H^* , the critical current of a type II superconductor depends on the magnitude of the pinning force that retards the motion of fluxons under the action of the Lorentz force.

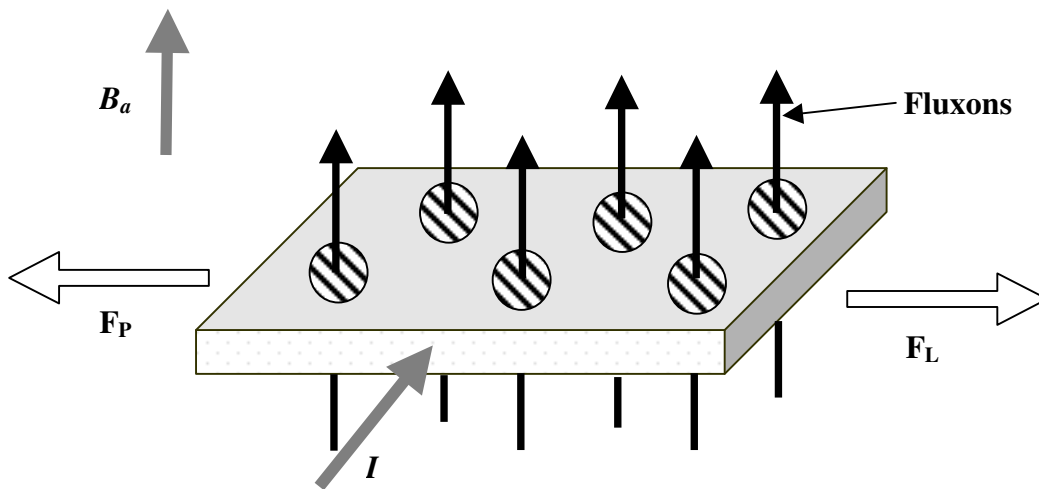


Figure 1.5 Flux lines in type II superconductors and the forces acting on fluxons in a applied field B_a with current I passing through it. The Lorentz force on the fluxons (F_L) is opposed by the pinning force (F_p). When $F_L > F_p$, the fluxons move and energy dissipation occurs.

CHAPTER 2

Nb₃Sn SUPERCONDUCTORS

2.1. Introduction

Superconductivity has been found in a wide range of materials, including pure metals, alloys, compounds, oxides, and organic materials. Out of these, the most practical materials for application at fields greater than 12 T are the intermetallic compounds (Type II superconductors) with the A15 crystal structure (discussed in next section). Table 2.1 summarizes the superconducting properties of these A15 compounds. Due to the superior properties and ease of manufacturing as compared to other A15 compound, Nb₃Sn is preferred for emerging applications requiring operation at high fields. Some of the important characteristics of Nb₃Sn compound are described in the following sections.

Compound	T_c (K)	H_{c2} (T) at 4.2 K
V ₃ Ga	14.8	19.5
V ₃ Si	17.0	22.5
Nb ₃ Sn	18.0	22.5
Nb ₃ Al	18.8	29.5
Nb ₃ Ga	20.3	33.5
Nb ₃ Ge	23.0	37.0

Table 2.1 Superconducting properties of the high field A15 compounds [23].

2.2. Properties of Nb₃Sn

2.2.1. Crystal Structure

Nb₃Sn possesses the brittle A15 crystal structure. The generic formula for an A15 crystal structure is represented as A₃B, in which the B atoms are arranged as a body center cubic crystal and two A atoms are centered on each face of the cubic unit cell, as illustrated in Figure 2.1. There are a total of 76 A15 crystalline compounds and 46 of them are superconductors. Typically, A atoms are a transition metal (i.e. Nb or V) and the B atoms are usually a group III or group IV element such as Sn, Ga, or Al [24].

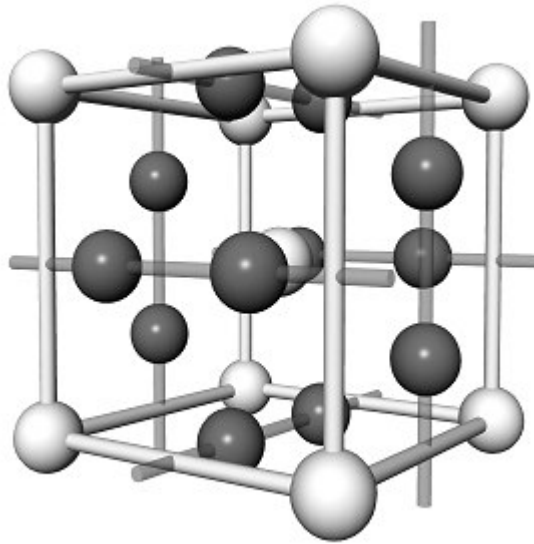


Figure 2.1 The A15 crystal structure of Nb₃Sn. Sn atoms (light spheres) forming a *bcc* structure and two Nb atoms (dark spheres) forming mutually orthogonal chains across the faces (reprinted from [25]).

For the stoichiometric composition the distance between two Nb atoms in the A15 lattice is about 0.265 nm with a lattice parameter of 0.529 nm [26]. This distance is about 0.021 nm less than that in the pure Nb *bcc* lattice causes a narrow peak in the d-band density of states (DOS) and forms a very high DOS near the Fermi level. This is believed to be the reason for the high T_c in A15 Nb₃Sn in comparison to *bcc* Nb [25].

2.2.2. Nb-Sn Phase Diagram

The phase diagram reported by Charlesworth *et al.* [27], is the generally accepted binary phase diagram for the Nb-Sn system (Figure 2.2). According to the phase diagram Nb has no solid solubility in the Sn and Sn has a maximum of 9 at% solid solubility at the peritectic temperature of 2130°C. The system consists of three intermetallic phases: NbSn₂, Nb₆Sn₅ and Nb₃Sn. The compounds NbSn₂ and Nb₆Sn₅ are stable in the stoichiometric composition only, whereas the compound Nb₃Sn is stable over a range from ~18 to ~25 at% Sn. Both NbSn₂ and Nb₆Sn₅ are non-superconducting at liquid helium temperature (4.2K), thus if these phases form during the heat treatment it is desired to convert these phases into the A15 Nb₃Sn phase. The Nb₃Sn is superconducting over much of its composition range and the superconducting properties (T_c , H_{c2} , and I_c) increases with the increase in the Sn composition. The critical temperature T_c varies from ~6 K at 18 at% Sn to ~18.3 K at 25 at% Sn [26]. At low temperature (≤ 43 K) and for composition above 24.5 at% Sn, the Nb₃Sn phase undergoes a cubic to tetragonal transformation which degrades the superconducting properties due to decrease in the density of states [26, 28, 29].

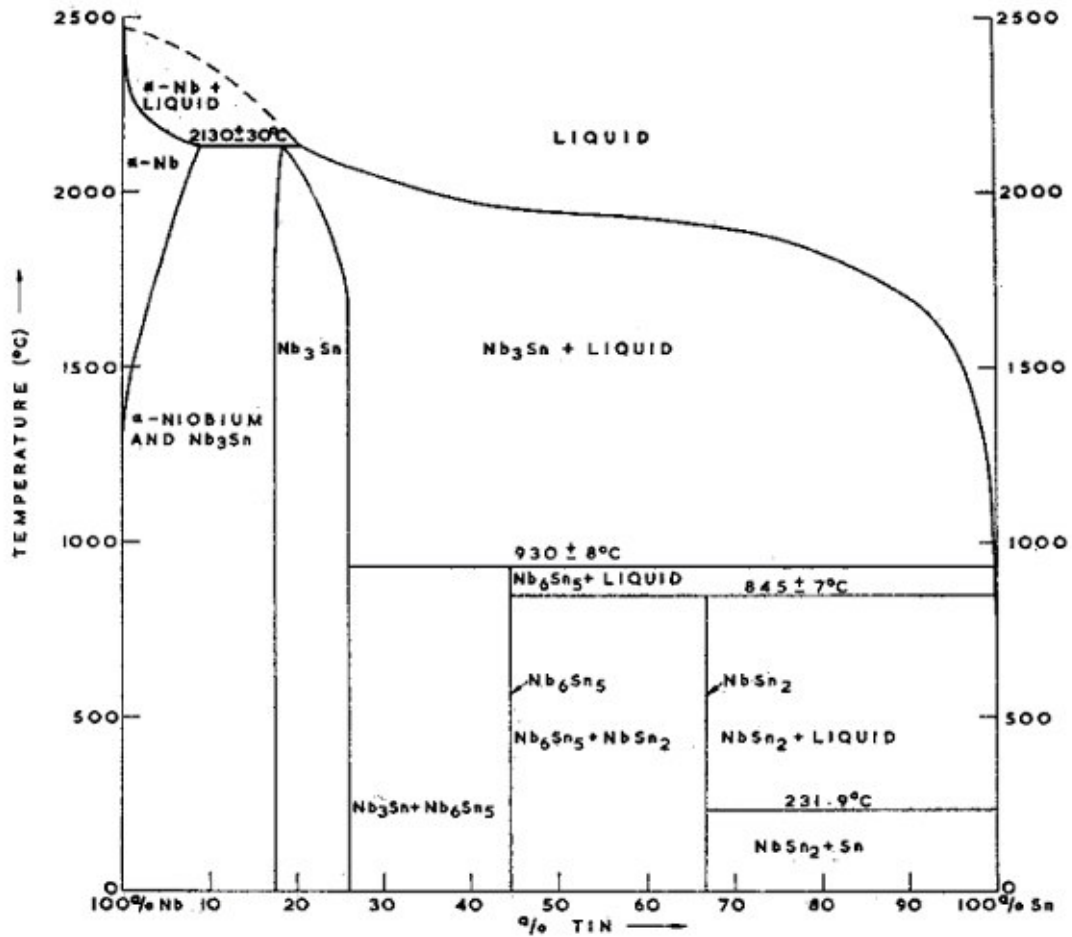


Figure 2.2 The Nb-Sn phase diagram (after Charlesworth [27]).

2.2.3. Dependence of H_{c2} and T_c on Sn Composition

As described in previous section, the Nb₃Sn A15 phase is stable over a composition range from 18 at.% to 25 at.% Sn. The superconducting properties T_c , and H_{c2} increase as the atomic Sn content increases in the A15 phase up to 24.5 at.% and above that the cubic to tetragonal transformation suppresses the properties. Figure 2.3 shows the trend in T_c and H_{c2} as a function of Sn composition along with the data from the literature. These plots are reproduced from a thesis on the subject by Arno Godeke [25].

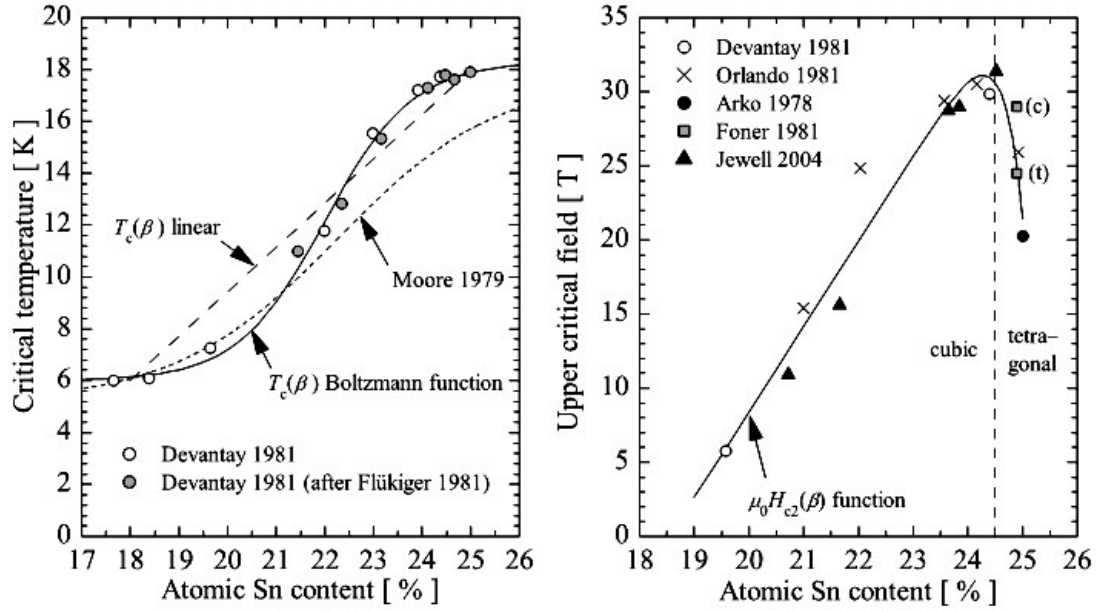


Figure 2.3 The critical temperature and critical field (at zero temperature) dependence on Sn composition. The solid curves represent best fit for the data. (reproduced from the work of Arno Godeke [25]).

A Boltzmann function best describes the trend in T_c [25] (shown as solid curve in the left plot in Figure 2.3.) as a function of Sn content, β :

$$T_c(\beta) = \frac{-12.3}{1 + \exp\left(\frac{\beta - 0.22}{0.009}\right)} + 18.3 \quad (2.1)$$

The highest reported value of T_c for the Nb_3Sn compound is 18.3 K [30]. The trend in the upper critical field H_{c2} is shown in the right plot in Figure 2.3. It is clear from the trend that the H_{c2} increases with the increase in the Sn content up to 24.5 at% and above that it starts decreasing due to the cubic to tetragonal phase transformation. The existing data on H_{c2} are summarized by an exponential and a linear fit by Godeke as a function of Sn composition, β :

$$\mu_o H_{c2}(\beta) = -10^{-30} \exp\left(\frac{\beta}{0.00348}\right) + 577\beta - 107 \quad (2.3)$$

Thus, a homogenous and stoichiometric Nb₃Sn phase is desired to achieve best superconducting properties. In recent years impressive improvements in the properties of Nb₃Sn have been reported. Nevertheless, further optimization seems possible. In this work the heat treatment steps are thoroughly examined and suggestions are made to decrease the compositional gradient in the Nb₃Sn phase.

2.2.4. Titanium and Tantalum Additions to A15 Nb₃Sn

It is well known that the superconducting properties of the Nb₃Sn conductors can be enhanced by the addition of ternary or tertiary elements. Past studies on the doping of Nb-Sn with ternary elements suggest Ti and Ta as the most effective additions for the enhancement of critical current density (J_c) and upper critical field (H_{c2}) [14, 31-36]. Tachikawa et al. [14] observed that small addition of Ti to Nb core in Bronze processed Nb₃Sn conductor not only accelerates the Nb₃Sn layer growth, but also enhances the upper critical field by up to 5 T. Ti significantly improved the critical current density at high field by enhancing upper critical field. Tachikawa concluded that the optimum amount of Ti in Nb core to be about 2 at. %.

At the same time Suenaga et al.[13] added Ti into expanded metal processed strands. They found out that at lower fields, Ti addition decreases J_c whereas at higher field the addition of Ti improves J_c . Suenaga et al.[13] also studied grain size. They believed the grain size increased due to adding Ti, which lowers the grain boundary pinning force in the low field, but in the high field, since the H_{c2} increase by the Ti

addition, improves its intrinsic superconductivity. Thus the high field J_c is still much better than the strands having no Ti addition. Suenaga's conclusion for grain size is worth further debating, since if Ti does accelerate Nb₃Sn formation rate, the strand with Ti is eligible to have a shorter heat treatment time to reach the same Nb₃Sn layer thickness as strand without Ti addition. In the case of Nb₃Sn, the grain size grows with longer heat treatment duration. Their heat treatment time were not specified and adjusted for Ti doped Nb₃Sn strands.

Around the same time (~1980), Ta was found to increase Nb₃Sn strand H_{c2} and also increase Nb₃Sn layer growth by Tachikawa et al. [14] and by Suenaga et al. [13]. There are two reasons known so far for Ti and Ta to increase H_{c2} values. First is that these ternary elements suppress the low temperature cubic to tetragonal transition for ≥ 2.8 at.% Ta or for ≥ 1.3 at.% Ti [37] which results in an increased $H_{c2}(0)$ while retaining $T_c(0)$. Secondly the normal state resistivity (ρ_n) increases with increasing Ti or Ta additions [37]. The relationship between H_{c2} and ρ_n is expressed as (Kim et al. [38]):

$$H_{c2}(0) = 3.11 \times 10^3 \cdot \rho_n \cdot \gamma \cdot T_c(0) \quad (2.4)$$

Where γ is the electron specific heat constant or Sommerfeld constant in J/m³K², ρ_n is normal state resistivity in Ω -m, T_c is in Kelvin and H_{c2} is in Tesla.

The H_{c2} , as measured in alloyed strands [35], increases with Ti or Ta additions and peaks at about 1.5 at%Ti or 4 at%Ta and then reduces with further increase in the alloy content. The initial increase in the resistivity by the Ti or Ta additions do not affect the $T_c(0)$ results in increase in H_{c2} with an increase in resistivity. However $T_c(0)$ starts to decrease above $\rho_n \approx 30\mu\Omega$ -cm and this itself diminishes H_{c2} [25].

Recent research has been focused on putting the optimum amount of Ta and Ti into Nb_3Sn system and exploring the right heat treatment conditions (temperature, stages and durations) to obtain the finest grain size, evenly distributed Sn, and optimal dopant concentration level. Pyon and Gregory [39] substituted Nb filaments with Nb-1.3 wt% Ti and Nb-7.5wt%Ta filaments in the internal-Sn type conductors. Recent work [40] on wires prepared by bronze route process showed that simultaneous addition of Ti and Ta were not helpful, however, this work was performed on bronze conductors, which have lower Sn content generally. Studies on internal-Sn conductors, on the other hand, have suggested improvements in J_c at high fields are possible [41].

As a practical matter, Ta has always been introduced as an alloying element into the Nb filaments (Nb7.5wt%Ta), while Ti has been introduced by several methods [42]. The earliest and most common method was to introduce Ti into the Sn core, usually as a metastable alloy. More recently it has been added in the form of Nb-Ti filaments replacing some of the Nb filaments in the billet [43]. Whatever the method, it is important to know what the optimum levels are (especially for conductors to be optimized for higher fields) as well as the influence of Ti on Sn diffusion and Nb_3Sn formation in high performance strands.

The kinetics, phase formation and morphology of grains of Ti and Ta doped Nb_3Sn bronze was investigated in recent publications. Layer growth kinetics for Ta doped Nb_3Sn bronze strand was determined by Pugh et al. [15, 16] using SEM combined with a low temperature inductive measurements. Pugh et al. agreed on that Ta refines the

grain size. On the other hand, Dieterich et al. [11] concluded that Ti does not have any effect on the Nb₃Sn grain size but influences the kinetics of Nb₃Sn formation.

In this work, the Sn core was alloyed with various amounts of Ti (0-2.8at %) and the filaments were made of Nb7.5 wt%Ta. Growth rate constants for the formation of Nb₃Sn have been determined for various level of Ti at three temperatures. The heat treatment schedule was designed to distribute Ti homogeneously and to optimize the high field J_c in conjunction with H_{c2} .

2.3. Manufacturing Methods

Nb₃Sn conductors can be manufactured by various processes. In this section the most commonly used fabrication methods are discussed. These are the Bronze process, the Internal –Tin process, and the Powder in Tube process.

2.3.1. The Bronze Process

The bronze process was the first viable wire manufacturing process [44]. In this method, the Niobium rods are inserted into a α -bronze matrix and then extruded and drawn down to the final diameter. A schematic of the cross section of the final wire is shown in the Figure 2.4. Although the bronze process is considered a reliable production route, it has few drawbacks. One is the work hardening of the bronze; therefore, frequent annealing steps (after every 50% reduction in size) are required during the drawing process. This makes process more labor intensive and during annealing there can be some possibility of the formation of the Nb₃Sn phase, which hampers further wire drawing. Another

drawback is the limitation on the amount of Sn in the Cu matrix. The amount of Sn is limited by the maximum solubility of Sn in Cu (~9.1 at %) as shown in the Figure 2.5.

After wire fabrication the wires are heat treated to form the Nb₃Sn phase by a diffusion reaction between Sn from the α -bronze and the Nb filaments. The advantage of this process is that a long piece (>2 km) can be manufactured with very small filament diameter (~5 μm) resulting in low hysteric loss (about 190 mJ/cm³ for ± 3 T loop [45]). However, wires processed by this method have low critical current density, the maximum critical current density achieved from these conductors is about 1000 A/mm² at 12 T and 4.2 K.

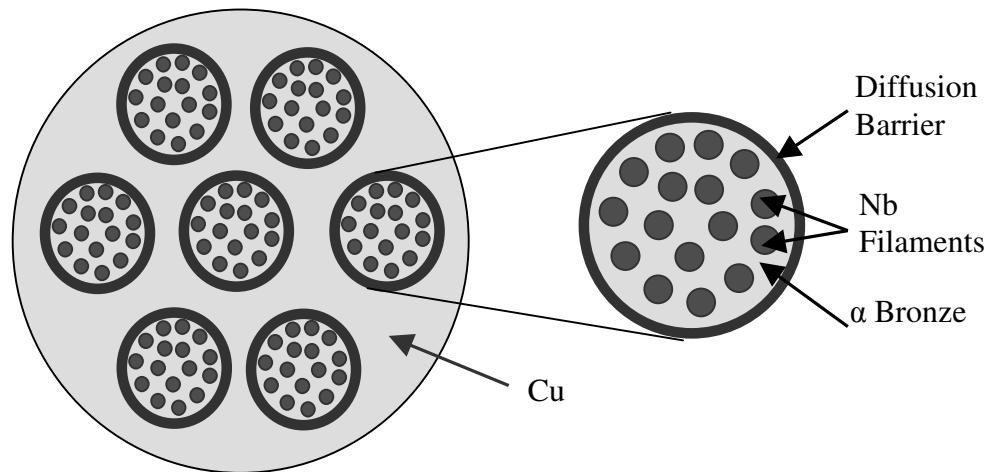


Figure 2.4 Schematic of cross section of a wire made by the bronze method.

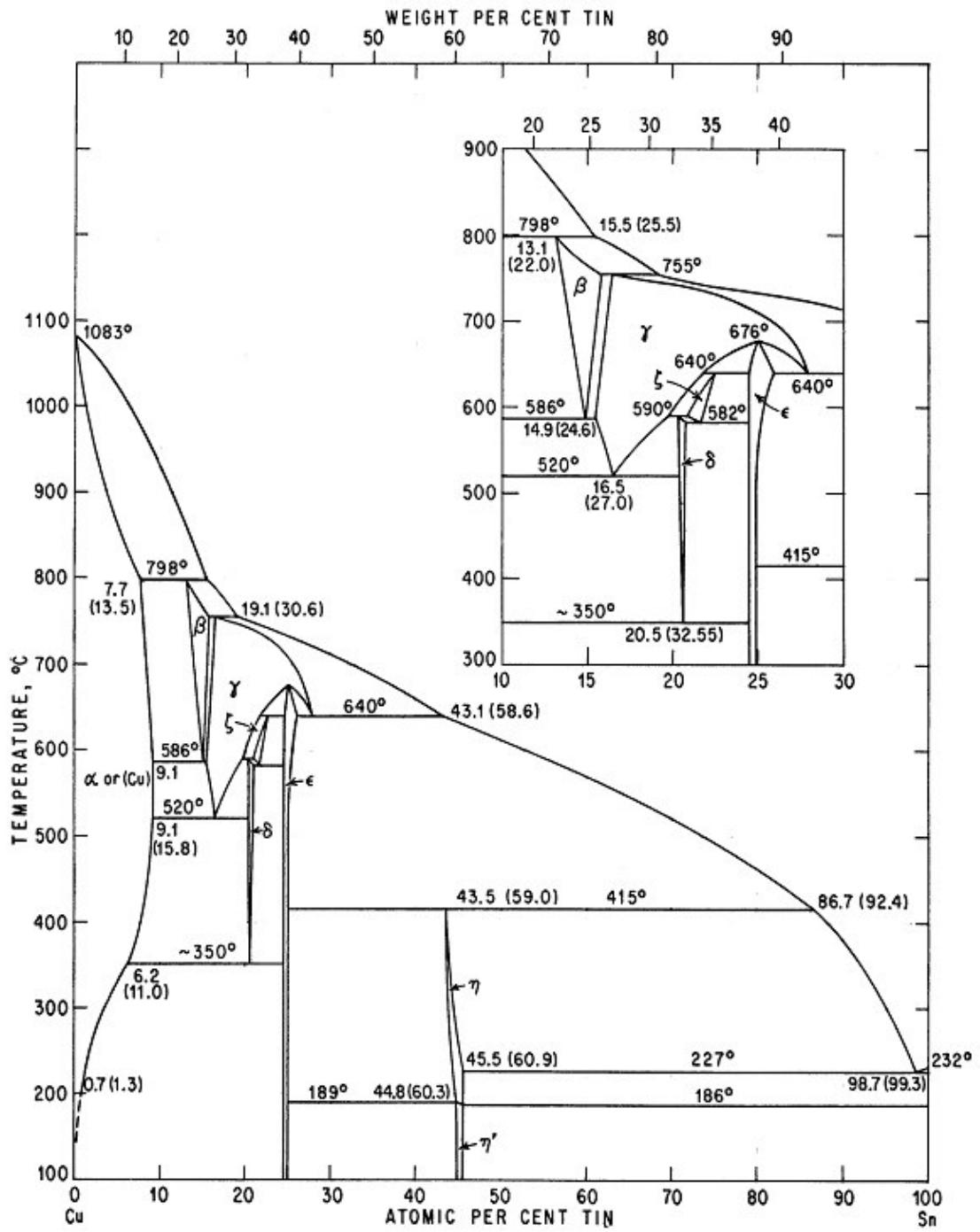


Figure 2.5 The Cu-Sn system (reproduced from [46])

2.3.2. The Internal Tin Process

The current density of the Nb_3Sn layer increases as the Sn concentration in the A15 phase increases [47]. Therefore, to overcome the limitation on the amount of Sn in the bronze process, a new process denoted 'Internal-Tin' was developed [48]. In this process a Sn source is inserted in the core and surrounded by Nb rods embedded in a copper matrix. In an earlier version of this process the subelements were put together in the center of the strand and surrounded by a single barrier, in the present day version each of the subelements is surrounded by diffusion barriers made of either Nb or Nb-Ta. A cross section of the wire manufactured by this process is shown in the Figure 2.6.

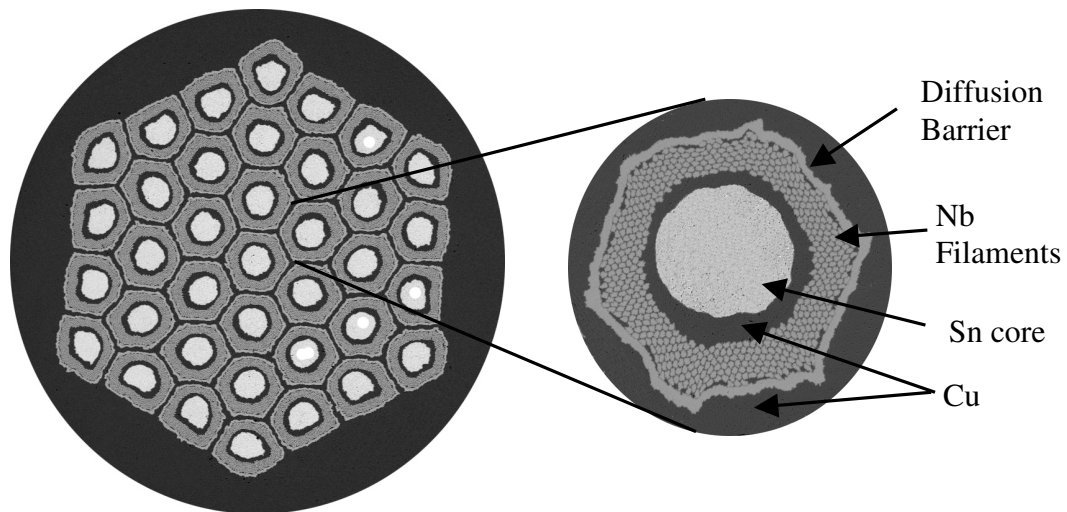


Figure 2.6 Cross-section of a wire made by the Internal-Tin process.

An early variant of this process was the Modified Jelly Roll (MJR) process, which had a slightly different manufacturing route, but very similar phase formation routes. In this process the Sn core is wrapped by two parallel sheets of Nb and Cu metals and then placed in the Cu tube to form a billet. The billet are then extruded and shaped as hexagonal rods which are then restacked in the form another billet. That billet is then drawn down to the final size. The steps involved in this process are illustrated in the Figure 2.7.

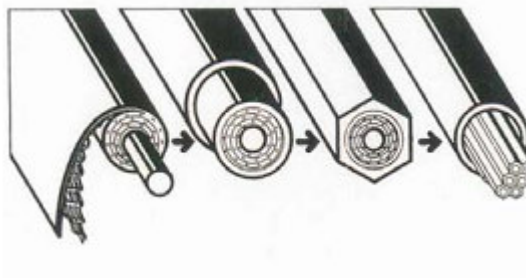


Figure 2.7 The Modified Jelly Roll process

The main advantage of the internal-tin process is the achievement of a higher Sn/Cu ratio as compared to that of the bronze process wire, results in a higher critical current density. Also, no annealing steps are required while drawing. The main drawback of this process is that extrusion is only possible during the sublement formation part of the process. One attempt to get around this problem was a Hot Extruded Rod process developed by Teledyne Wah Chang Company, in which NaCl fillers replaces Sn during the extrusion. After extrusion the NaCl is dissolved creating a hole into which Tin rods are placed. However, this solution never became practical. Another drawback of the internal-tin process is the bridging in between the Nb filaments which results in

electromagnetic coupling of the filaments which causes a higher hysteretic loss [49] and magnetizations which are too large for certain applications. The maximum current density achieved from the internal-tin processes wires is about 3000 A/mm^2 at 12 T and 4.2 K in final, restacked strands.

2.3.3. The Powder in Tube process

In this process hollow Nb tubes are filled with a powder (NbSn_2 , plus additives) and then placed into a Cu matrix [50]. Cross section of a wire manufactured by the Powder in Tube process is shown in Figure 2.8.

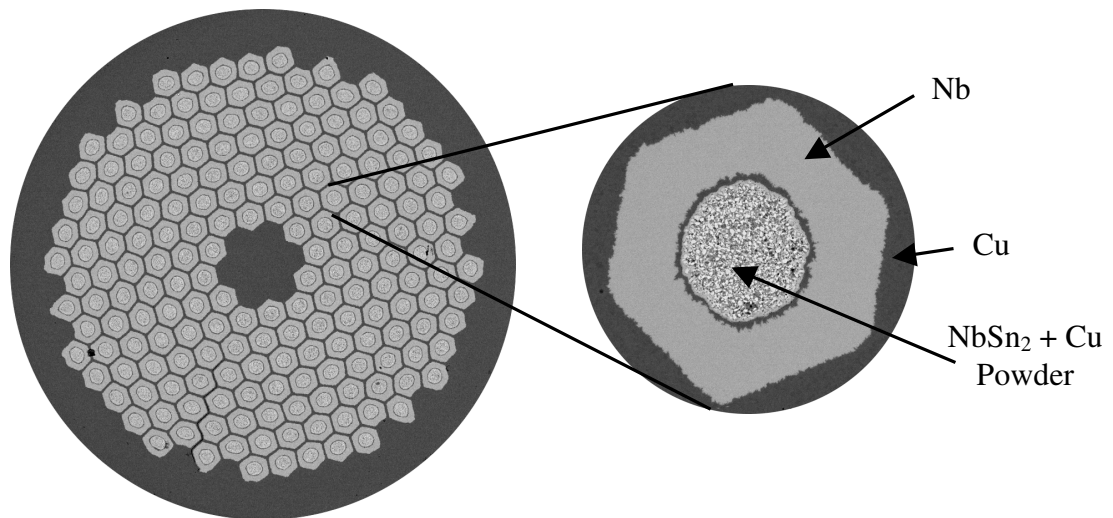


Figure 2.8 Cross section of a wire made by the Powder in Tube process.

The powder in tube process has several advantages over other techniques. One is the shorter heat treatment time, as the Sn source is located near to the Nb, it does not require pre-reaction heat treatment as compared to the internal-tin process. Another

benefit is that well separated smaller (30-50 μm) filaments could be achieved which results in low hysteric loss. The drawback of this type of conductors is the higher cost, as the Nb tubing and specialty powders are expensive, and it is difficult to control the powder size, which is crucial to the manufacturability of these conductors. To overcome some of these problem a new method termed as “Tube-Type” was developed by Gregory et al.[51]. The tube-type sublements can be pictured as a standard internal-Sn sublements but with its annulus of Cu-clad Nb rods replaced by a Cu-lined Nb tube. The maximum non-copper critical current density achieved from these types of conductors is about 2500 A/mm^2 at 12T and 4.2 K.

Among all of the above processes, the internal tin processed wires are the most commonly used for applications in high field magnets due to their high current carrying capacity (J_c). The current work presented in thesis was also carried out on the internal-tin type conductors to further enhance their current capacity.

CHAPTER 3

SAMPLES PREPARATION

3.1 Sample Specifications

3.1.1 Samples for Cu-Sn Diffusion Study

To investigate the diffusion of Sn in the Cu matrix of the Nb_3Sn conductor, four different types of internal-tin type subelements were used. Samples denoted EG23 and EG24 were manufactured by Supergenics LLC while two others denoted GL28 and GL29 were manufactured by Global Research Incorporation, Columbus. Back scattered electron (BSE) images of the cross sections of these conductors are shown in the Figures 3.1-3.4. The composition of filaments and the barrier varied among these strands. Subelement EG23 had Nb7.5Wt% Ta with no Ti, while in EG24 Ti was added as foil wraps around individual filaments (Figure 3.2). GL28 had pure Nb filaments, and added Ti as Nb47%Ti rods. GL29 had Nb7.5wt%Ta rods with Ti added as Nb47%Ti.

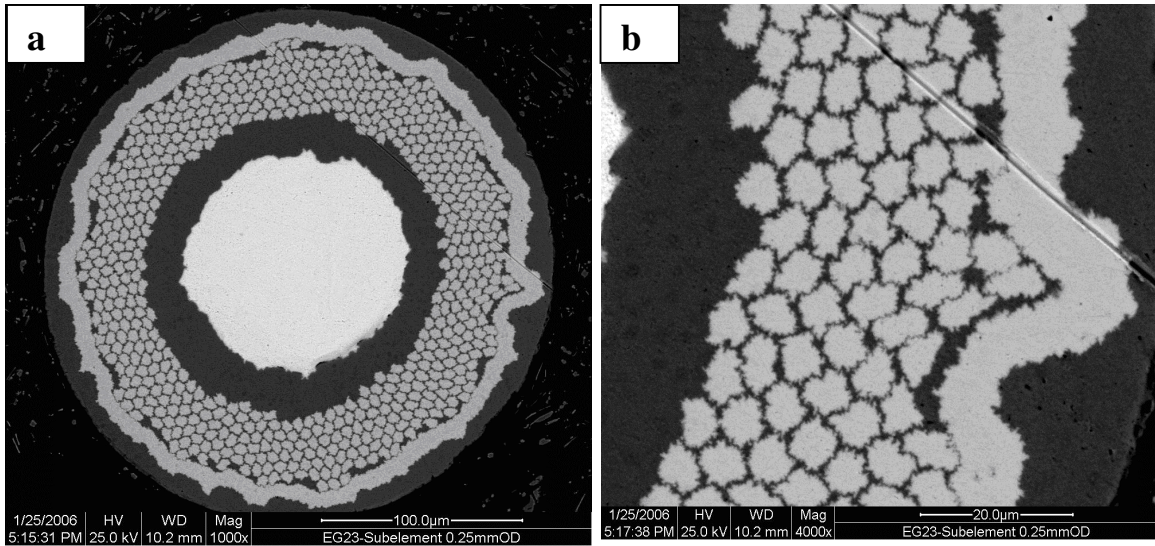


Figure 3.1. SEM-BSE images of sample EG23 (a) the cross-section of the sample, wire diameter 0.25 mm (b) Higher magnification of the filaments and the barrier; both are made of Nb 7.5 wt% Ta.

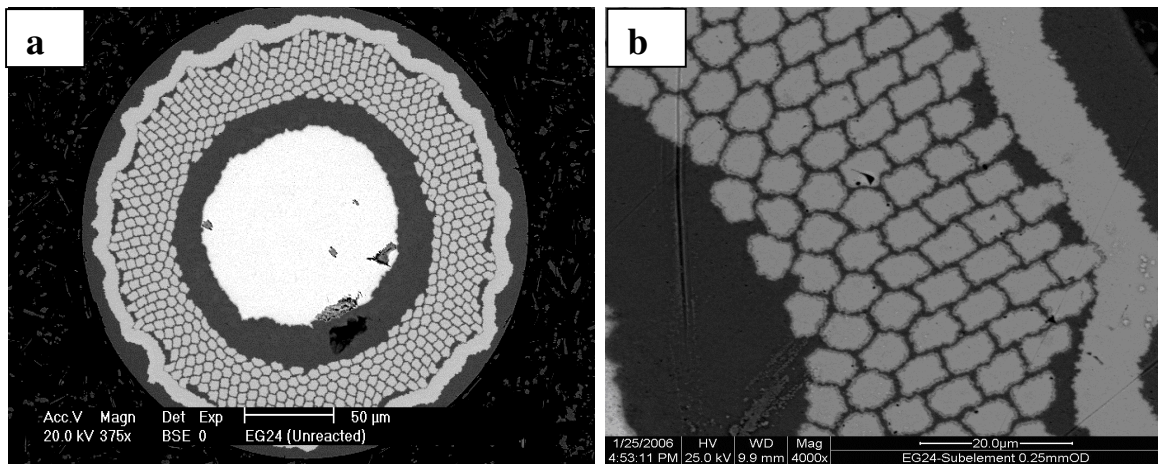


Figure 3.2. SEM-BSE images of sample EG24 (a) the cross-section of the sample, wire diameter 0.25 mm (b) Higher magnification of the filaments and the barrier both having composition of Nb7.5wt%Ta, additionally all the filaments were wrapped with Nb47%Ti sheath.

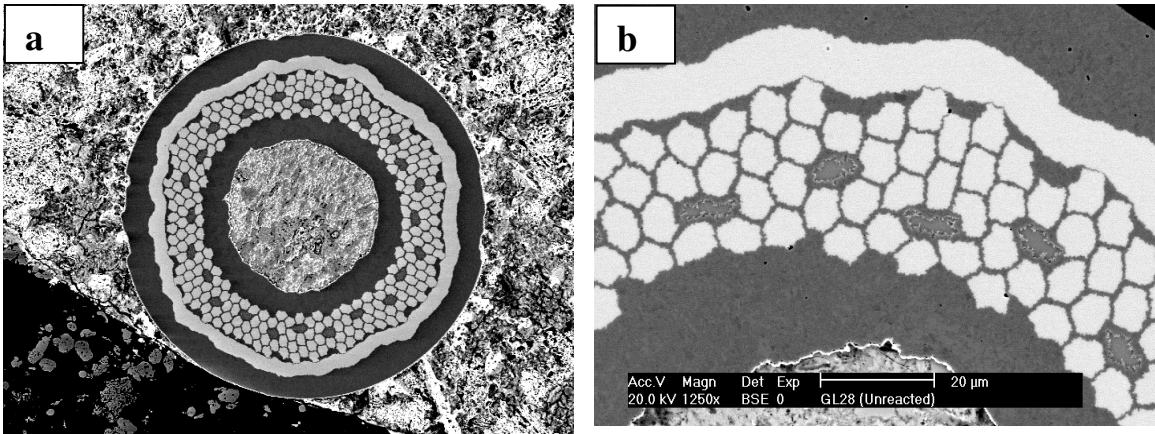


Figure 3.3. SEM-BSE images of sample GL28 (a) the cross-section of the sample, wire diameter 0.25 mm (b) Higher magnification of the filaments and the barrier. Filaments and barrier are made of pure Nb except the few filaments as seen in the image with slightly gray contrast are made of Nb47%Ti.

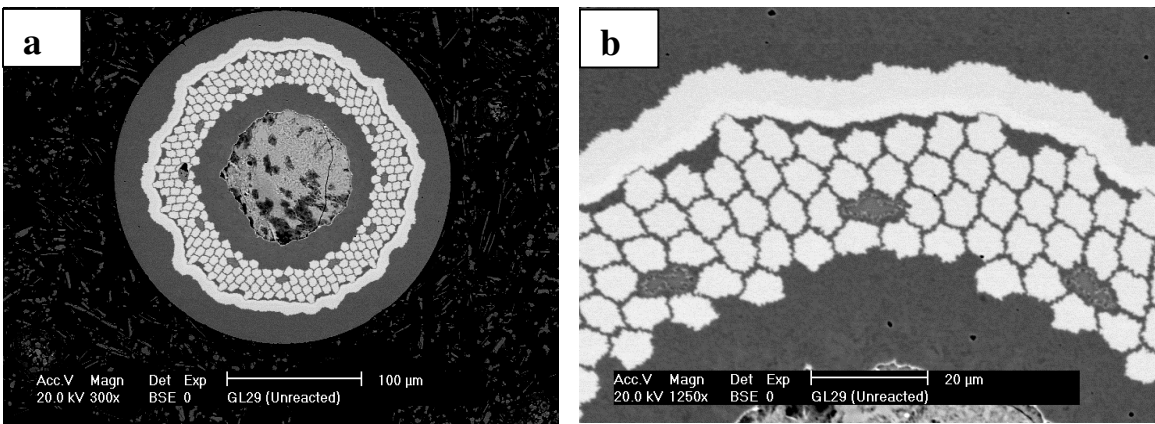


Figure 3.4. SEM-BSE images of sample GL29 (a) the cross-section of the sample, wire diameter 0.25 mm (b) Closer look of the filaments and the barrier. Filaments and barrier are made of Nb7.5wt%Ta, except the few filaments as seen in the image with slightly gray contrast are made of Nb47%Ti.

A detailed description of each of these strands is given in Table 3.1. The area fractions of the Sn, Nb, and Cu shown in Table 1 were determined by counting the corresponding pixels in the cross-sectional image of these samples using an image analysis software package [52] (The procedure is discussed in section 4.2).

Strand Name	EG23	EG24	GL28	G129
Fil No./Comp	588/ Nb7.5Ta	588/Nb7.5Ta+W NbTi ^a	264/Nb + 24 /Nb47Ti	276/Nb7.5Ta +12/Nb47Ti
Barrier Comp	Nb7.5Ta	Nb7.5Ta	Nb	Nb7.5Ta
A_{Nb}/A_{Cu} array	85/15	80/20	71/29	81/19
R_{Sn0} , μm	55	55	50	48
$R_{Array, ID}$, μm	74	73	68	67
$R_{Array, OD}$, μm	108	108	97	94
A_{Nb}^b/A_{Sub}	0.399	0.388	0.30	0.280
A_{Sn}/A_{Sub}	0.187	0.194	0.170	0.146
A_{Cu}/A_{Sub}	0.35	0.357	0.470	0.519
A_{Nb}/A_{Sn}	2.134	2.0	1.765	1.91

^aNb47%Ti sheath wrapped around the filaments.

^bArea included all the filament area and half of the barrier area.

Table 3.1 Specifications of samples for Cu-Sn diffusion study.

3.1.2 Samples for the Study of Effect of Ti Addition

To examine the effect of Ti addition on the growth rate of Nb₃Sn phase and the properties of the conductors (B_{c2} , and J_c), four types of internal tin type subelements were used. These conductors were manufactured by Global Research Incorporation in Columbus, OH. As described previously, Ti can be added by various methods. In these strands the Ti was introduced into the core using commercially available Sn-2wt%Ti rods. Core of

these sublements consisted of an assemblage of pure Sn and Sn-2wt% Ti rods to give an overall Ti level (within the core) ranging from 0 at% to 2.8 at%. The SEM-BSE images of the cross-section of these samples are shown in Figures 3.5 and 3.6.

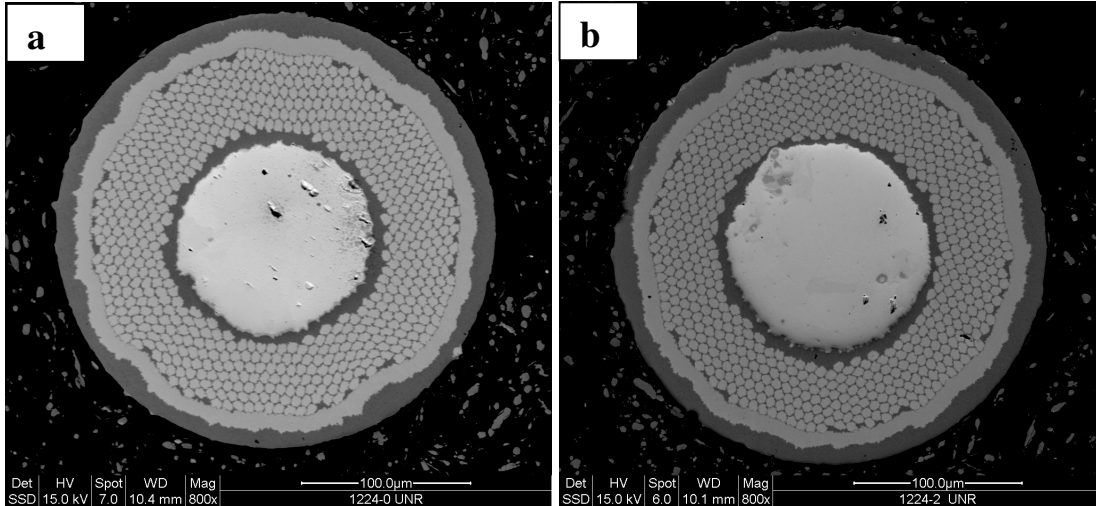


Figure 3.5. Internal-tin type sublements (a) sample G0 with pure Sn core (b) sample G2 with 1.4 at% Ti in core.

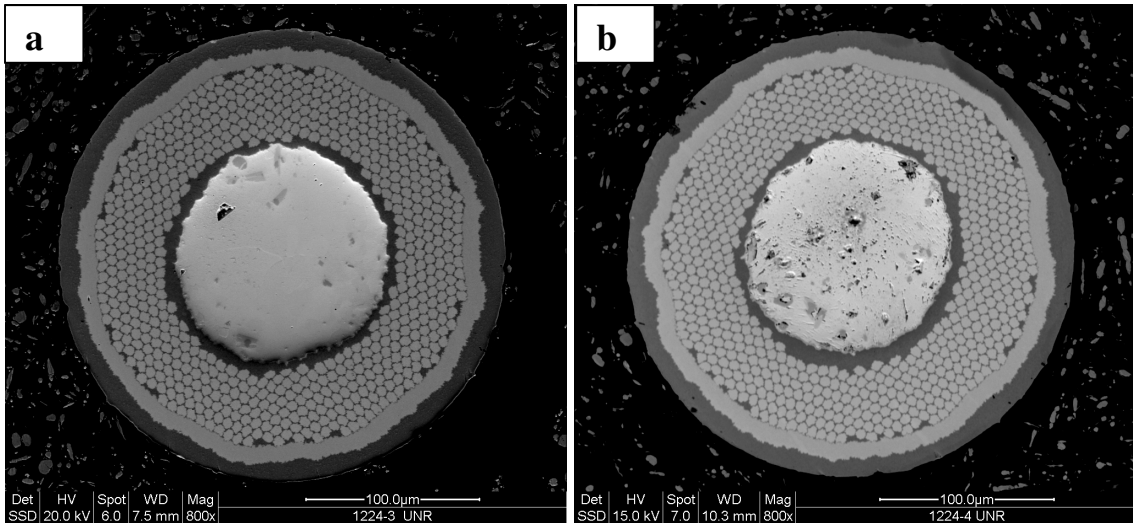


Figure 3.6. Internal-tin type sublements (a) sample G3 with 2.1 at% Ti in the core (b) sample G4 with 2.8 at% Ti in the core.

The filaments in these four strands were made of pure Nb and the barrier composition was Nb7.5wt%Ta. Table 3.2 gives detailed description of each of these strands.

Strand Name	G0	G2	G3	G4
Tracer ID	1224-0	1224-2	1224-3	1224-4
Ti Level in Core (at %)	0	1.4	2.1	2.8
Ti Target level in Nb ₃ Sn (at %)	0	0.35	0.53	0.70
Barrier Composition	Pure Nb	Pure Nb	Pure Nb	Pure Nb
Filament Composition	Nb 7.5wt%Ta	Nb 7.5wt%Ta	Nb 7.5wt%Ta	Nb 7.5wt%Ta
No. of Filaments	629	629	629	629
Filament Diameter (μm)	~6.5	~6.5	~6.5	~6.5
Barrier Thickness (μm)	10.5	10.5	10.5	10.5
A_{Cu}/A_{Sub}	0.083	0.093	0.101	0.088
A_{Nb}/A_{Sub}	0.537	0.491	0.484	0.494
A_{Sn}/A_{Sub}	0.209	0.234	0.241	0.234

Table 3.2 Specifications of samples for the study of effect of Ti addition.

3.2 Heat Treatment

As described in the Chapter 2, internal-Sn Nb₃Sn strands are manufactured as composites of Cu, Nb, and Sn. These composites are then heat treated to form the A15 Nb₃Sn superconducting phase. The heat treatment sequence varies depending upon the strand design and the composition. A typical heat treatment for the internal tin type strand is shown in the Figure 3.7. The heat treatment is usually divided into three steps. As the pure Sn has low melting point (~232°C), the strands are initially ramped up to a temperature lower than the melting point of Sn, to avoid the formation of liquid in the

core of the strand. Typically, in the first step the temperature is ramped up to 210°C with a ramp rate of 10°C/hr and held for 48 hours. Then in the second step the temperature is raised up to an intermediate temperature (~400°C) with a ramp rate of 25°C/hr and held for 48 hours. At the end of the second step the Sn is almost homogeneously distributed in the Copper matrix. An insignificant amount of Nb reacts with Sn up to this temperature range and therefore the heat treatment up to this step is called 'pre-reaction' heat treatment. In the third step and final step in the heat treatment the Sn starts diffusing into Nb and forms Nb₃Sn. The temperature in the final step is above 640°C and it is held for various times to optimize the amount of Nb₃Sn phase. The heat treatment temperature and duration for this final step is designed in such a way that the all the Nb in the filaments along with half of the barrier width is converted to Nb₃Sn. It is important not to react too long, however, such that it is possible to avoid leakage of Sn into the Copper matrix outside the barrier. All of the Nb₃Sn formation takes place in the final step (the reaction portion) of the heat treatment and therefore the final step is usually called the 'reaction' heat treatment.

To heat treat these strands, segments of 30 cm in length were encapsulated in quartz tubes under a 0.25 atmospheric pressure of Argon. The ends of the strands were pre-torched to avoid the Sn-leak during the heat treatment. A tube type furnace with programmable controller was used to heat treat the strands.

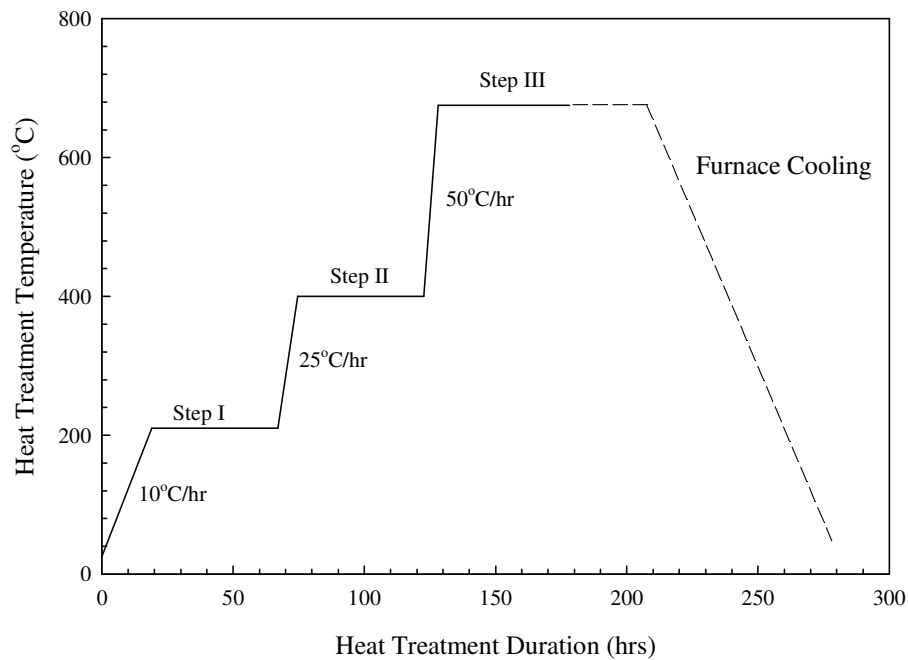


Figure 3.7 Typical heat treatment for the internal-tin type strands.

3.3 Sample Preparation for Electron Microscopy

Sample preparation for scanning electron microscopy (SEM) mainly involves two steps, the first step is the mounting of the sample in a mold and the second is the polishing. The mounting of the wire samples could be done using an air setting epoxy mixed with conductive carbon powder or by using a heat setting conductive Bakelite powder. The first method is usually called *cold mounting* while the second is called *hot mounting*. For cold mounting the epoxy, hardener, and conductive carbon powder were mixed in a ratio of 5:1:6. Stainless steel clips were used to hold the wire in a vertical position. After air drying for 6-8 hrs, the mold becomes rigid and can be polished. Figure 3.8(b) shows a cold mounted sample. This type of mold is usually not preferred for scanning electron

microscopy because of the presence of many voids on the surface of the mold and the poor electrical conductivity through the mold. However, the cold mounting was used for non-heat treated samples as the hot mounting may result in initiation of the diffusion of Sn in the Cu matrix.

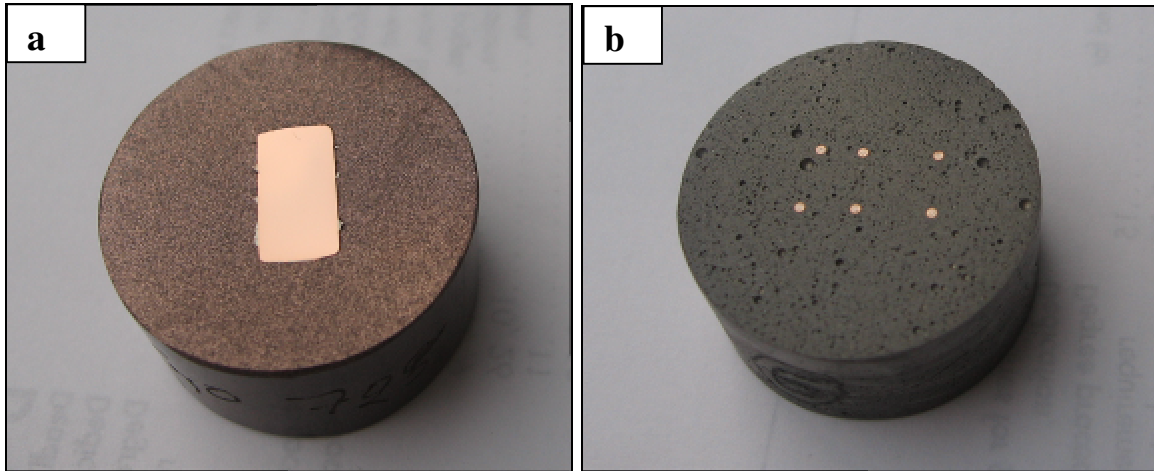


Figure 3.8. Samples mounted for SEM; (a) Hot mounted sample (b) Cold mounted sample.

For hot mounting, the wire samples are first soldered onto a Cu block and then placed in a press along with conductive Bakelite powder. The Bakelite is heated while a constant pressure is maintained. This results in a dense, conductive, rigid mold. Hot mounting (Figure 3.8(a)) was for samples which were already heat treated.

After mounting the sample, the molds were then polished to obtain a smooth surface finish. Initial polishing was performed using SiC abrasive papers with grit size starting from 320 to 1200. After polishing with 1200 grit size paper, the molds were cleaned ultrasonically and then placed in a vibrating polisher in which colloidal silica

(0.05 micron) was used as as a polishing media. After polishing for 5-6 hours the molds were removed from the polisher, ultrasonically cleaned and air dried.

CHAPTER 4

EXPERIMENTAL METHODS

4.1 Introduction

In this chapter the experimental techniques used for the microstructural analysis, critical current and critical field measurements are discussed. A brief introduction about the instruments and techniques is included at the start of the each section.

4.2 SEM, EDS, and Image Analysis

In scanning electron microscopes (SEM), the electrons are emitted from a source and accelerated towards the specimen surface. These electrons after striking the surface of the specimen scatter through the specimen within a defined volume called the interaction volume. The electron beam-specimen interaction produces secondary electrons, backscattered electrons, X-rays, and heat. A schematic of the electron beam-specimen interaction is shown in the Figure 4.1.

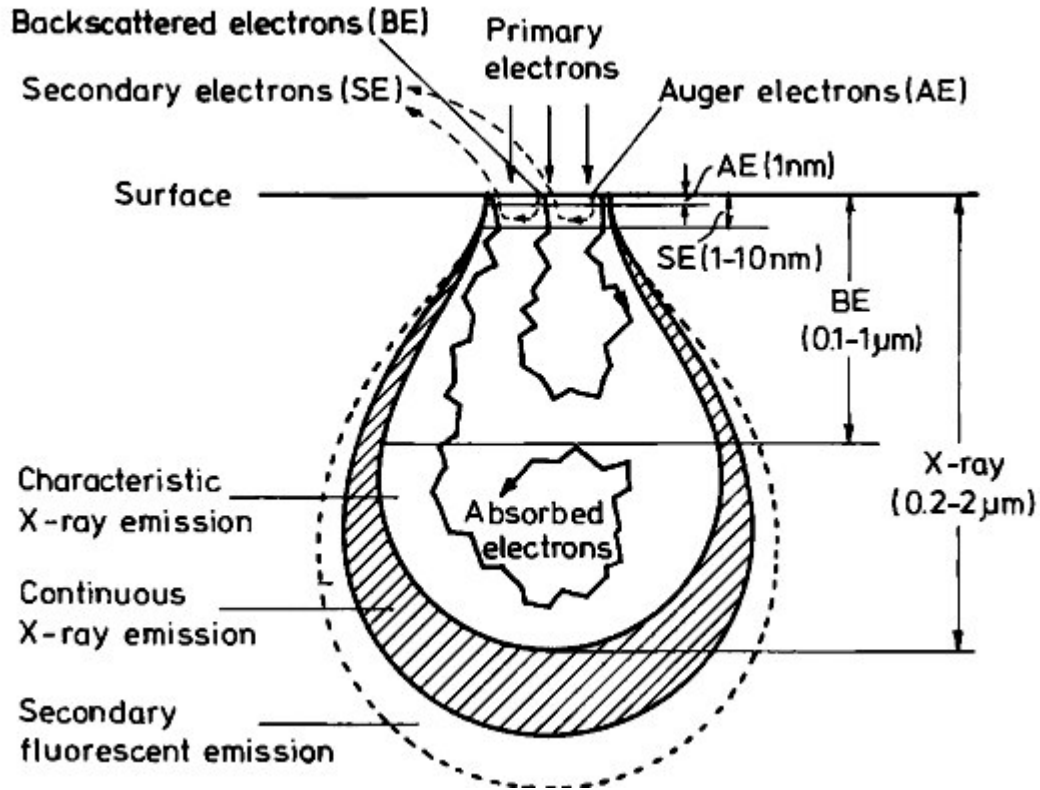


Figure 4.1. Products of the interaction of the electron beam and the specimen and the depth of information in scanning electron microscope. (The fluorescence emissions can come from as deep as 100 μm) (reprinted from [24]).

The secondary electrons mainly contain the information of the surface structures. A secondary electron detector collects these electrons and use for the imaging. The secondary electron image is mainly used to detect any surface defects. On the other hand back scattered electrons (BSE) are produced deep within the specimen and have much higher energy. The contrast in the image produced by using these electrons is based upon the atomic number of the elements and their arrangement. BSE-images are therefore used to analyze the various phases present in the specimen. As mentioned earlier that the interaction of electron beam-specimen results in X-rays of various wavelength. Since

each element emits X-rays of particular wavelength that are characteristic for that element alone, the sorting of these X-rays allows us to establish the presence of various elements in the specimen. Also, the intensities of these X-rays are used in quantitative analysis. When X-rays are sorted on the basis of energy, the technique is called Energy Dispersive Spectroscopy (EDS). For the accurate measurement of the composition in a particular area of the specimen, it is important to ensure that all the X-rays signal collected by the detector are generated from that area only. Therefore it is essential to know the shape and size of the electron beam-specimen interaction region (i.e. interaction volume).

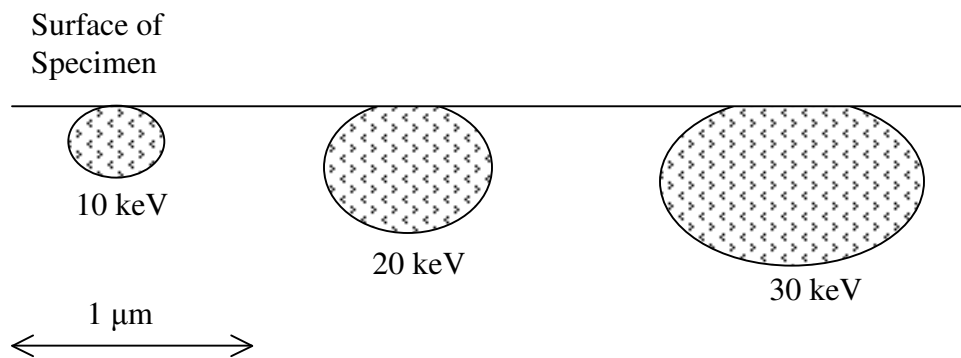


Figure 4.2. Showing the shape and size of the specimen-beam interaction volume in a specimen of iron with an electron beam at 10-,20-, and 30-kV accelerating voltages.

The shape of the specimen-beam interaction volume depends on the atomic number of the specimen and the energy of the beam electron. Higher the energy of the electron is, the greater the penetration. The number of inelastic events increases as the energy of the beam electrons increases, resulting in less deflection of the electron beam

on scattering and deeper penetration of the electrons into the solid [53] (Figure 4.2). In low atomic number specimens the beam electrons undergo three times as many inelastic as elastic collisions, the deflection of the beam electrons is small and a pear shaped specimen-beam interaction volume results. Whereas in the higher atomic number specimens, a greater number of elastic collisions occur when the electron beam initially strikes the specimen, resulting in greater deflection of the electrons in the specimen. The specimen-beam interaction zone is without the neck characteristic of the low atomic number (Figure 4.3.) Also, the beam electrons do not penetrate to as great a depth as they do in specimens of low atomic number, because the mean free path between collisions is shorter in higher atomic number specimens and there are more elastic collisions.

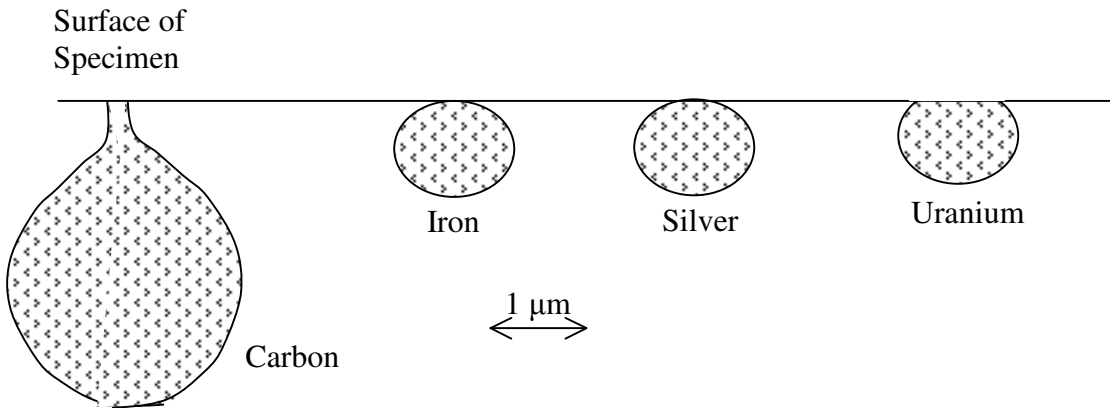


Figure 4.3 Shape and size of the specimen-beam interaction volume in specimens of different atomic number. Accelerating voltage is 20 kV[53].

The interaction volume for the Nb₃Sn specimen was calculated by using the Monte-Carlo simulation. To keep the interaction volume minimum as well as to get sufficient signal out of the specimen, an accelerating voltage of 15 kV was used for the

energy dispersive spectroscopy (EDS). The interaction volume in Nb₃Sn specimen with 15 kV accelerating voltage was approximately 1 μm in depth. (Figure 4.4)

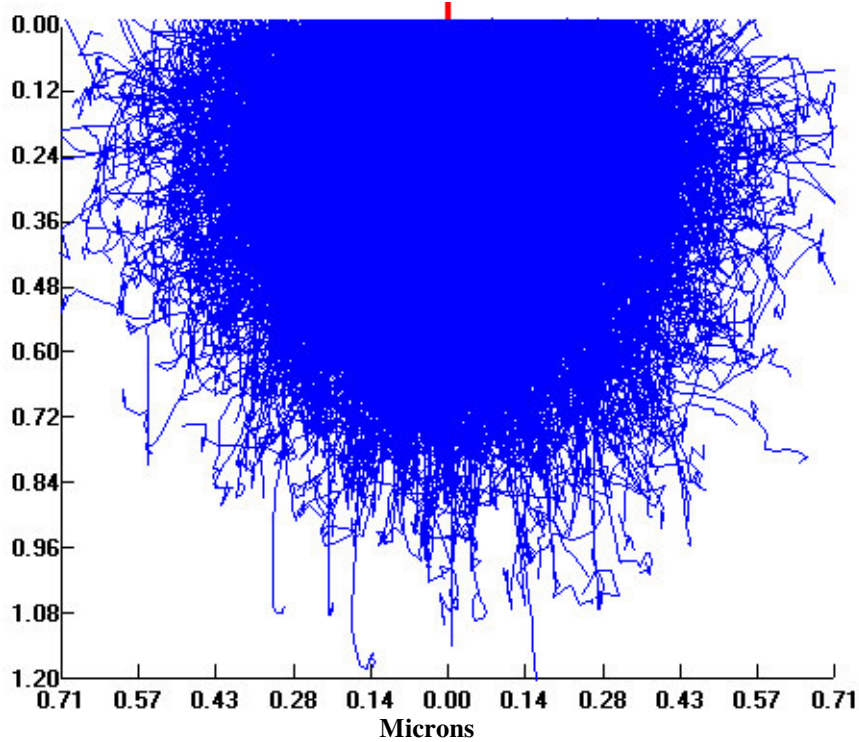


Figure 4.4 Monte-Carlo simulation showing the interaction volume for the Nb₃Sn specimen with accelerating voltage of 15 kV (No. of trajectories: 32000).

In the present work all the SEM studies were made using FEI Quanta 200 SEM and Philips XL-30 ESEM, both with Energy Dispersive Spectroscopy attachment. For EDS analysis the instruments were calibrated with a homogenous, and stoichiometric (25 at% Sn) bulk Nb₃Sn sample [54].

After obtaining the BSE images, the Sn, Cu and Nb area fractions were determined using image analysis tools Adobe Photoshop and Image Tool [52]. The BSE images have good atomic number contrast; therefore various phases can easily be differentiated. Image Tool was used to convert the images into binary images (black and

white) and to count the pixels. Figure 4.5 shows a BSE image of the crosssection of the superconducting subelement and the corresponding converted binary images of the various portions of the subelement. The area fraction of Nb, Sn and Cu can be determined by counting the corresponding pixels from these images. Also these area fractions can be converted into atomic fraction by multiplying with the atomic densities.

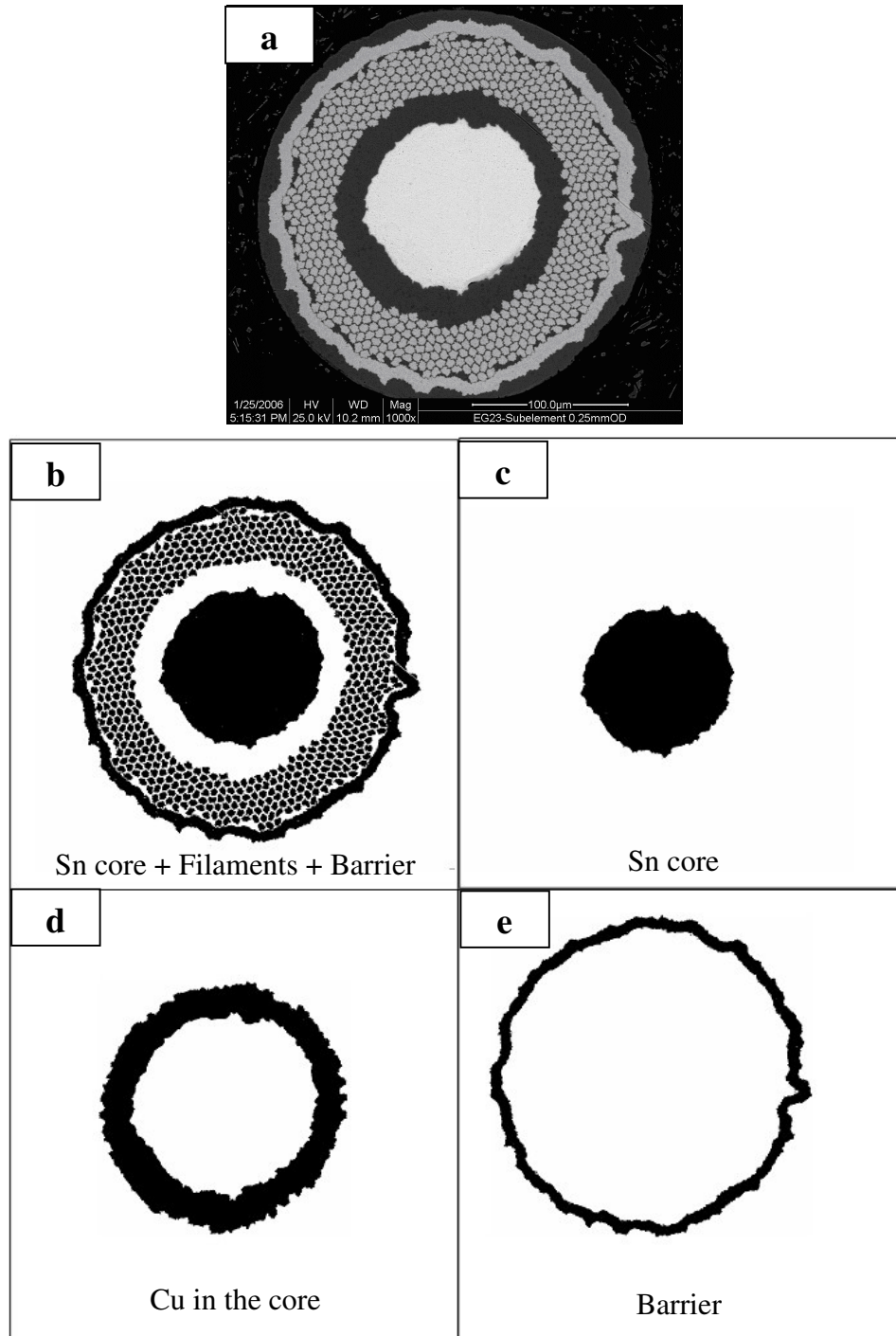


Figure 4.5 (a) The SEM-BSE images of the superconducting subelement, (b) The converted binary image of the subelement (c,d,e) separated sections of the Sn core, Cu and the barrier respectively.

4.3 Critical Current Measurement

The critical current I_c , of various specimens were measured (data presented in Chapter 6), by the methods described below. For short sample I_c measurements, superconducting wires (diameter 0.25 mm) 2.5 cm long were mounted on a 1mm thick Cu plate using Sn-Pd solder. The copper plate was then attached to a probe as shown in the Figure 4.6. The current was supplied to the specimen by the Cu rods which were attached electrically to a power supply. The voltage taps (gauge length 0.5 cm) were then made to measure the voltage across the sample. After mounting the sample the probe is initially cooled in a liquid N₂ Dewar and then inserted into the bore of a superconducting magnet, which is inside a liquid helium cryostat. The cryostat consists primarily of a vacuum insulated cylindrical bore containing a superconducting magnet at the bottom. The superconducting magnet can be ramped up to 15 T at liquid helium temperature (4.2 K). The cryostat is filled with liquid helium and then the probe is inserted into the cryostat. A current supply is attached to the probe externally and the current is passed through it at various fields ranging from 10 T to 15 T. The voltage across the sample is measured as a function of current at a particular field.

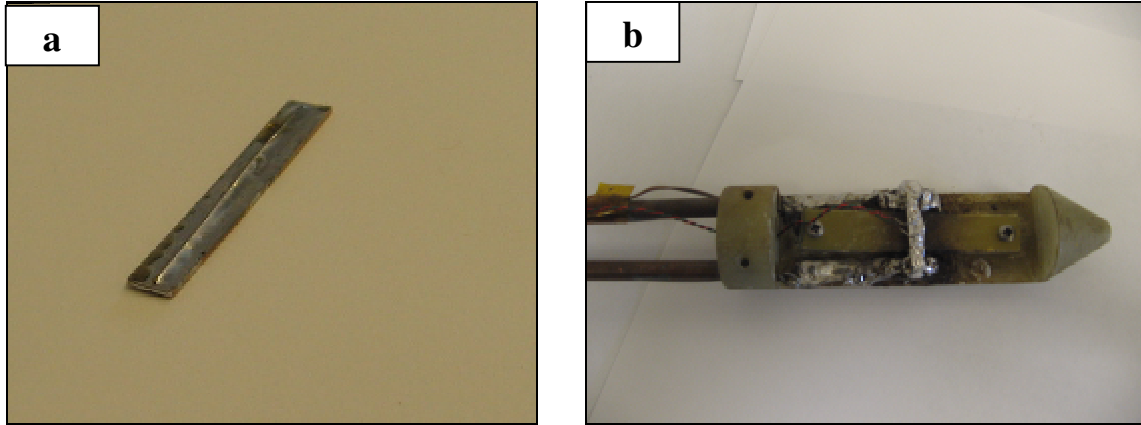


Figure 4.6 (a) Short sample (2.5 cm long, diameter 0.25 mm) mounted on Cu plate (b) The Cu plate attached to the short sample measurement probe.

4.4 Upper Critical Field (B_{c2}) Measurement

The upper critical field B_{c2} , is the one of the three characteristics which defines the critical state of superconductors. For Nb_3Sn the typical value of the critical field is about 25 T. The upper critical field is measured by passing a small, constant current through the specimen and by measuring the resistance across the wire in a varying magnetic field. These measurements were carried out at the National High Magnetic Field Laboratory (NHMFL) in Tallahassee, Florida. Standard Sn-Pb solder was used for all the contacts and the distance between the voltage taps was 0.5 cm. The sample length was 1cm and sensing current of 10 mA was used. All the measurements were done at 4.2 K in an applied field ranging from 0 to 33 T. The field was applied perpendicular to the sample length. A 90% resistive criterion was used to extract the B_{c2} values from the resistivity-magnetic field curve. Figure 4.7 is a typical resistivity vs magnetic field curve. Data obtained in this way are discussed in Chapter 6.

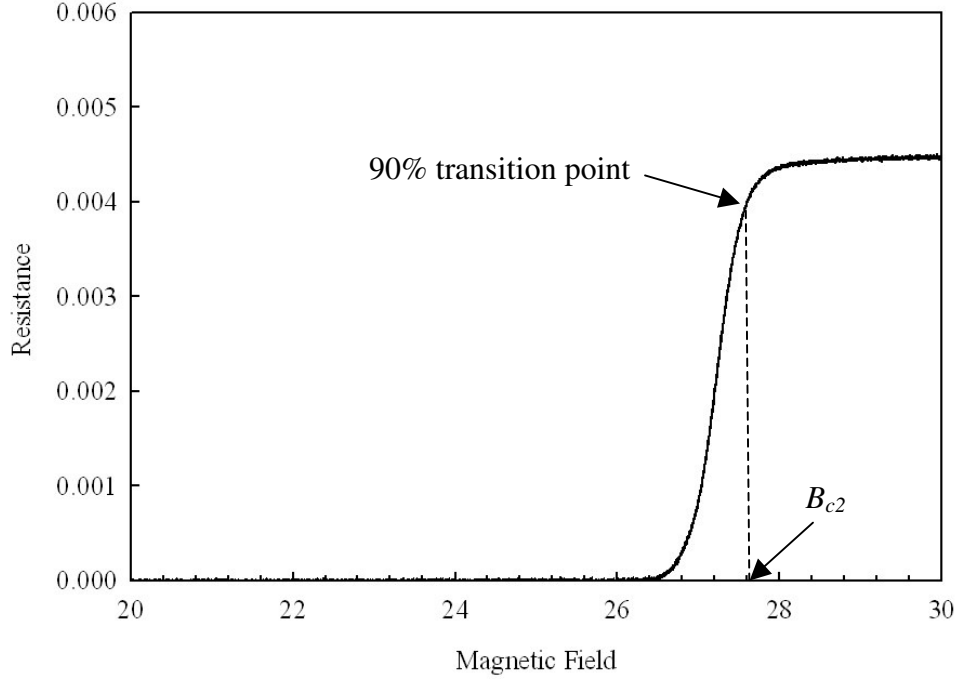


Figure 4.7 A typical resistivity vs magnetic field curve for Nb_3Sn superconductors.

CHAPTER 5

MEASUREMENTS OF DIFFUSION AND PHASE FORMATION

5.1 Introduction

In the following sections the formation of Cu-Sn intermetallics and Nb₃Sn phase during the various stage of the heat treatment are described for internal-tin type Nb₃Sn strands.

5.2 Intermetallic Formation

Intermetallic formation is realized by the formation and growth of at least one new phase due to diffusive interaction between two initial phases. In the simplest case of interaction between a metal A and a metal B, only one intermetallic phase A_mB_n is formed at the interface. Two contrary viewpoints are usually discussed with regard to the mechanism of this process [55]. According to first viewpoint, an intermetallic phase can appear only when the solubility limit of the solid solution is attained at the boundary layer of the solvent metal at a given temperature:



That is the phase A_mB_n appears diffusively (D) as a result of a phase transformation (FT) in a supersaturated solid solution.

The second viewpoint postulates that intermetallics are formed as a result of a chemical reaction at the interface of reacting metals, irrespective of their mutual solubility. The preparatory state in the forming of a new metallic phase at the interface is chemisorption (CS), i.e. an adsorption in which chemical forces of interaction are developed:



The second scheme is really justified only when there is a total mutual insolubility of the components [56].

Now considering the growth kinetics of intermetallics that are of substantially different composition from the matrix, the rate of growth can be described by the following relation [56]:

$$G = \frac{\partial y}{\partial t} = \alpha B_i \frac{1}{N} \frac{\partial \phi}{\partial y} \quad (5.3)$$

Where α is the geometric factor, B_i the mobility of substitutional atoms i in the matrix, N is the number of atoms at a constant molar volume and, $\partial\Phi/\partial y$ is the gradient of thermodynamic potential in the direction of growth. Using only the chemical part of the change in thermodynamic potential (i.e. $\partial\Phi/N = \partial\mu_i$) and the following well known thermodynamic dependences:

$$B_i = \left(\frac{D_i}{kT}\right) \left(\frac{\partial \ln C_i}{\partial \ln a_i}\right) \quad \text{and} \quad \partial\mu_i = kT \partial \ln a_i$$

Then from equation (5.3) we get

$$G = \frac{\partial y}{\partial t} \approx \alpha D_i \frac{\partial \ln C_i}{\partial y} = \alpha D_i \frac{\partial C_i}{C_i \partial y} \quad (5.4)$$

After certain simplifications ($\alpha = 1$; $\partial C_i / \partial y \approx \Delta C / y$; D_i and ΔC are constant), it follows that

$$\int_{t_0}^t y dy = \int_{t_0}^t D_i \frac{\Delta C}{C_i} dt \quad (5.5)$$

When $t = t_0$, the thickness of intermetallic compound (y) is equal to zero, hence

$$y^2 = 2D_i \frac{\Delta C}{C_i} (t - t_0) = k(t - t_0) \quad (5.6)$$

Where k is the layer growth rate parameter.

When $t \ll t_0$, equation 5.6 reduces to Tammann and Rocha's [57] well known expression for growth rate:

$$y = k' \sqrt{t} \quad (5.7)$$

When the conditions that allow such simplifications are not justified, in particular, if D_i and ΔC are not constant, then the time dependence of y deviates from the parabolic law.

In the general case, the layer growth is [56, 58]:

$$y^n = k(t - t_0) \quad (5.8)$$

Where the temperature dependence of the growth rate parameter k is given as:

$$k = k_0 \exp(-E / \beta T) \quad (5.9)$$

Where k_0 is a constant, T is the temperature, β is the Boltzmann constant, and E is the activation energy.

In this work the layer growth equations (5.7) and (5.8) have been used extensively to predict the thicknesses of the Cu-Sn and Nb₃Sn intermetallic phases during various stages of heat treatment.

5.3 The Cu-Sn System

As discussed in Chapter 3, the purpose of pre-reaction heat treatment for these conductors is to distribute the Sn in the Cu matrix prior to the start of reaction heat treatment and Nb₃Sn formation. Therefore, it becomes necessary to understand the diffusion of Sn and systematics of the Cu-Sn intermetallic formation during the early stage of the heat treatment ($T < 415^\circ\text{C}$). The Cu-Sn binary phase diagram is shown in Figure 5.1 [46]. In the Cu-Sn system the phases which appear upon initial heating of Sn-Cu interface are the Sn-rich Cu₆Sn₅ (η) and Cu-rich Cu₃Sn (ϵ). As the temperature of heat treatment increases the thicknesses of these intermetallics increase. The first liquid appears at temperature $> 227^\circ\text{C}$. The Sn melts at temperature of 232°C . The solubility of Sn in Cu also increases with temperature up to 520°C . The maximum solubility of Sn in Cu is about 9.1 at% in the temperature range of $520^\circ\text{C} - 586^\circ\text{C}$. The Cu₆Sn₅ phase melts at temperature of 415°C . Also seen in the phase diagram is the appearance of a Cu₄₁Sn₁₁ (δ) phase at temperatures above 350°C . Though predicted by the phase diagram the phase is not observed until the temperature reaches 500°C [59]. For the internal tin type conductor the pre-reaction heat treatment is performed below 415°C . Therefore, the present work is focused only on the

formation of the Cu_3Sn (ϵ), and Cu_6Sn_5 (η) phases in the temperature range 185°C to 400°C .

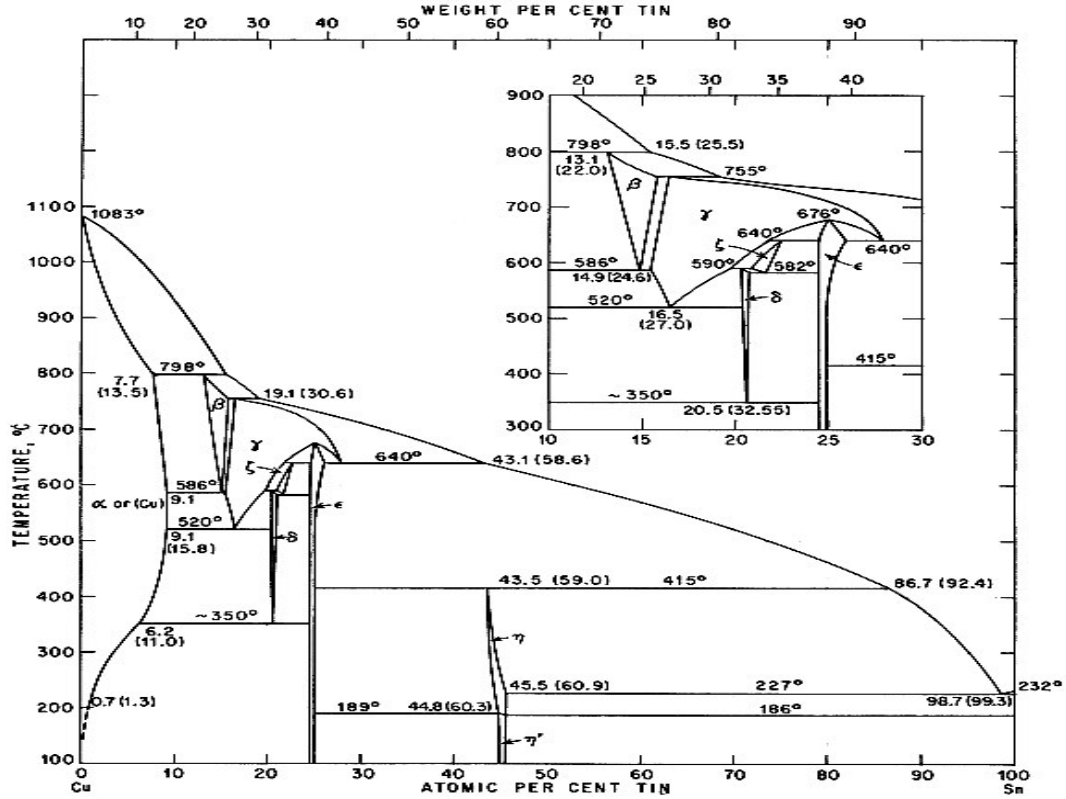


Figure 5.1 The Cu-Sn system (reproduced from [46]).

5.4 Growth Rates of Cu-Sn Intermetallics

In this section the evolution of Cu-Sn intermetallics during the pre-reaction heat treatment of the subelements is examined. The growth rate parameters for these intermetallics are obtained. Four different types of strands as described in Section 3.1.1 were given a series of heat treatments to observe the growth of the Cu-Sn intermetallics.

The heat treatment schedule is shown in Table 5.1. After each of the heat treatment (HT) steps the cross-section of the samples were examined via SEM. Phases were identified by EDS measurements and the thicknesses of these phases were computed using image analysis software (Section 4.2).

Step No. (ramp rate)	Step I (10°C/hr)	Step II (25°C/hr)
1 Temperature/Duration	210°C/48hr	400°C/0hr
2 Temperature/Duration	210°C/48hr	400°C/12hr
3 Temperature/Duration	210°C/48hr	400°C/18hr
4 Temperature/Duration	210°C/48hr	400°C/24hr
5 Temperature/Duration	210°C/48hr	400°C/48hr

Table 5.1. The pre-reaction heat treatment schedule for four different types of subelement EG23, EG24, GL28 and GL29.

As predicted from the Cu-Sn phase diagram the diffusion of Sn into the Cu matrix leads to the formation of Cu_3Sn (ϵ) and Cu_6Sn_5 (η) phases at the Cu-rich and Sn-rich boundaries respectively, as shown in the Figure 5.2. At temperatures below the melting point of Sn (<232°C) the diffusion of Sn is very slow. Even after 48 hrs at 210°C the η and ϵ phases have reached thicknesses of only 2.5 μm and 3.0 μm , respectively. During the second HT step the Sn melts and faster diffusion occurs. Figure 5.3 shows the growth

of the η and ε phases after 24 hr and 48 hrs at 400°C. As seen in the cross-section after 48 hrs at 400°C the ε phase has grown into the filamentary array region and the Sn in the core has almost been depleted.

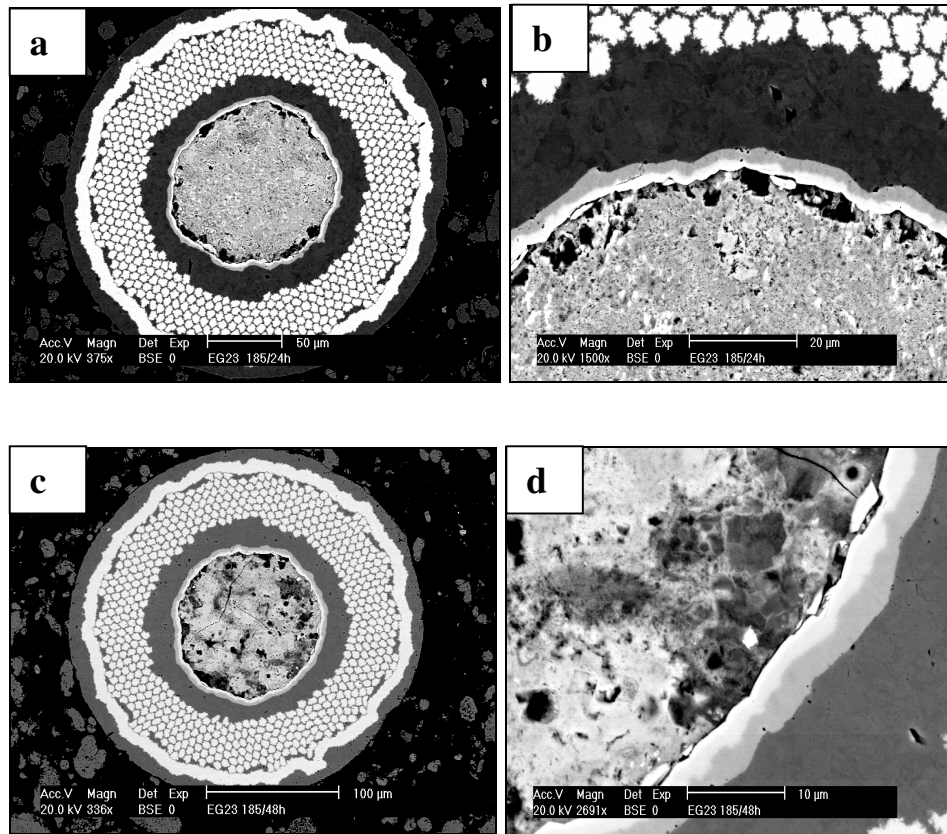


Figure 5.2. BSE-SEM examination of the growth of the ε and η phases in EG23 during the first step of the heat treatment at: (a) and (b) 210°C after 24 hrs; (c) and (d) 210°C after 48 hrs.

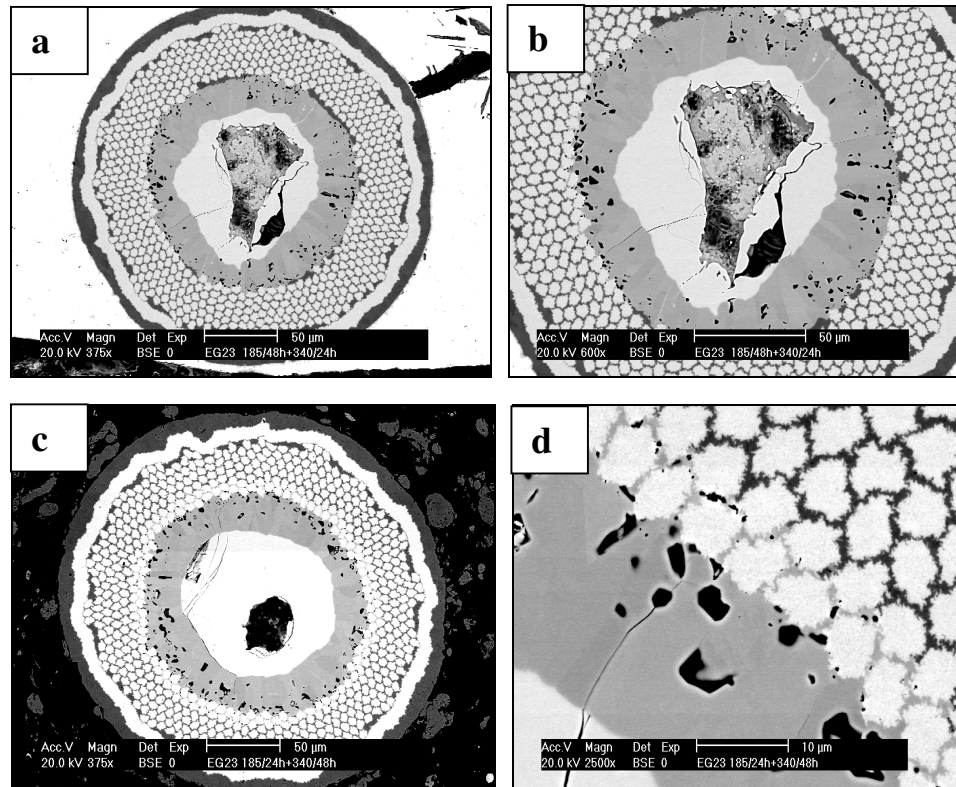


Figure 5.3. BSE-SEM showing the growth of the ϵ and η phases in EG23 during the second step of the heat treatment for (a) and (b) 24 hrs at 400°C; (c) and (d) 48 hrs at 400°C.

The parabolic growth law as described in Section 5.2 was then used to fit the growth layer data. The fitted equation is given as:

$$y^2 - y_o^2 = k(T) \cdot t \quad (5.10)$$

Where y is the thickness of the intermetallic layer at time t , y_o is the initial thickness (at time $t = 0$) of the intermetallic layer and k is the growth rate constant at temperature T . Figure 5.4 shows the linear fit between the square of the layer thickness and time. The growth rate parameters obtained from the slope of these fits are listed in the Table 5.2.

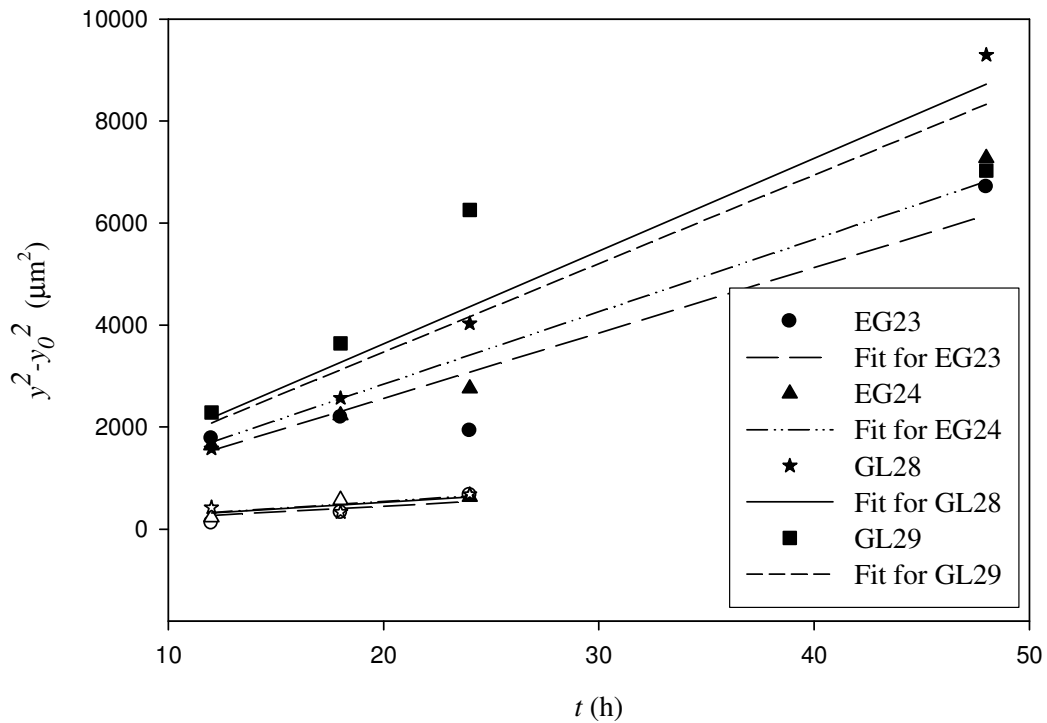


Figure 5.4. Growth of η and ϵ phases during pre-reaction heat treatment at 400°C for each type of strand. (Solid symbols: ϵ phase, Open symbol: η phase). η phase layer growth is shown before the depletion of Sn occurs. η phase growth data for GL29 has not been included here as the Sn depletion in this strand occurs just after 12 hrs at 400°C.

Strand Name	k_η ($10^{-14}\text{m}^2/\text{s}$)	k_ε ($10^{-14}\text{m}^2/\text{s}$)
EG23	0.62	3.56
EG24	0.75	3.94
GL28	0.73	4.00
GL29	-	4.82

Table 5.2 Growth rate parameters for η and ε phases at 400°C.

These growth rate constants are useful to predict the thicknesses of the η and ε phases as a function of time. However, knowing the rate of layer growth is not enough to determine the radial positions of these phases during the heat treatment. In order to optimize the heat treatment it is needed to know the radial positions of these phases as a function of temperature and time. Therefore, a simple analytical method was developed to predict the radial positions of the η and ε phases as a function of time and temperature. The model is described in the next section.

5.5 Analytical Model

5.5.1. The Model

The uniformity in the final A15 Nb₃Sn phase composition as compared between filaments at different radial positions within the subelements depends on the homogeneity of the Sn composition in the Cu matrix prior to the start of the formation of Nb₃Sn. Therefore, to optimize the distribution of Sn in Cu matrix it is desired to know the radial position of the Cu-Sn intermetallic during the pre-reaction heat treatment.

As stated earlier a typical heat treatment includes three steps. An initial low temperature step (150°C-227°C) is followed by an intermediate step (350°C-550°C), and finally a reaction heat treatment (650°C-675°C). During the first step of the heat treatment the Sn remains in the solid state, and a simple mass balance equation is used to find a relationship between the radial positions of Sn core, η and ε phases. A schematic representation of the radial positions of these phases is shown in the Figure 5.5.

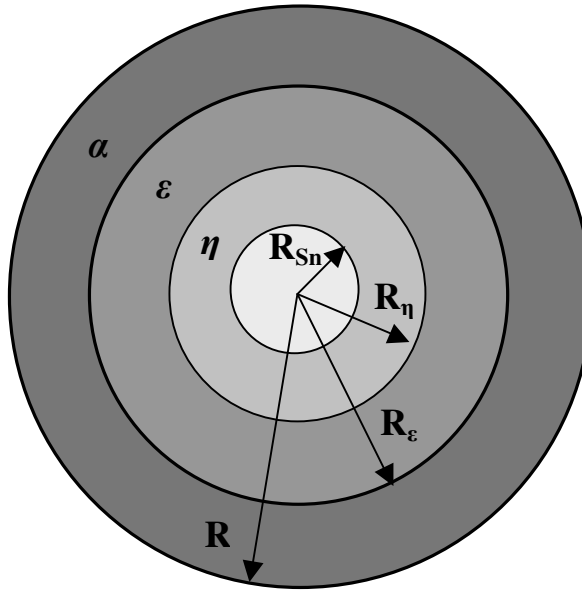


Figure 5.5 Schematic of strand geometry showing the radial growth of η and ε phases after some time t during the pre-reaction heat treatment.

In the temperature range of 150°C-227°C the solubility of Sn in Cu is negligible. Hence, the amount of Sn in α phase (Cu-Sn solid solution) can be ignored. Balancing the mass of Sn in the rest of the phases gives the following relationship:

$$\begin{aligned} \pi R_o^2 \rho_{Sn} &= \pi R_{Sn}^2 \rho_{Sn} + \pi (R_\eta^2 - R_{Sn}^2) \rho_\eta w_\eta^{Sn} \\ &+ \pi (R_\varepsilon^2 - R_\eta^2) \rho_\varepsilon w_\varepsilon^{Sn} \end{aligned} \quad (5.11)$$

Where R_o is the initial radius of the Sn core; R_{Sn} , R_η and R_ϵ are the outer radii of the Sn core, η and ϵ phases respectively at time t (Figure 5.5); ρ_{Sn} , ρ_η and ρ_ϵ are the densities of the pure-Sn, η and ϵ phases respectively; w_η^{Sn} , and w_ϵ^{Sn} are the average weight fractions of Sn in the η and ϵ phases respectively. All are in SI units.

Now the parabolic layer growth law (Equation 5.6) for the layer growth of the η and ϵ phases can be written as:

$$y_\eta^2 = (R_\eta - R_{Sn})^2 = k_\eta(T) \cdot t \quad (5.12)$$

$$y_\epsilon^2 = (R_\epsilon - R_\eta)^2 = k_\epsilon(T) \cdot t \quad (5.13)$$

Where y_ϵ and y_η are the layer thicknesses of the η and ϵ phases respectively after time t ; k_η , and k_ϵ are the growth rate constants for the η and ϵ phases respectively.

Now substituting the value of the R_η and R_ϵ from equation (5.12) and (5.13) into (5.11) and solving for R_{Sn} gives:

$$\begin{aligned} R_{Sn}^2 + 2R_{Sn} \sqrt{t} \left(\sqrt{k_\eta} \frac{\rho_\eta}{\rho_{Sn}} w_\eta^{Sn} + \sqrt{k_\epsilon} \frac{\rho_\epsilon}{\rho_{Sn}} w_\epsilon^{Sn} \right) \\ + t \left(k_\eta \frac{\rho_\eta}{\rho_{Sn}} w_\eta^{Sn} + k_\epsilon \frac{\rho_\epsilon}{\rho_{Sn}} w_\epsilon^{Sn} + 2\sqrt{k_\epsilon k_\eta} \frac{\rho_\epsilon}{\rho_{Sn}} w_\epsilon^{Sn} \right) - R_o^2 = 0 \end{aligned} \quad (5.14)$$

By plugging in the values of k_η , and k_ϵ (at the heat treatment temperature of interest) along with the densities of the various phases (Table 5.3), an analytical expression for R_{Sn} as a function of time can be obtained from Equation 5.14. Then the

expression for R_{Sn} along with Equations (5.12) and (5.13) can be used to find expressions for R_η and R_ε respectively.

$\rho_\varepsilon = 9.14 \cdot 10^3 \text{ kg/m}^3$	$k_\varepsilon(210^\circ\text{C}) = 7.30 \cdot 10^{-17} \text{ m}^2/\text{s}$	$w_\varepsilon^{Sn} = 0.38$
$\rho_\eta = 8.45 \cdot 10^3 \text{ kg/m}^3$	$k_\eta(210^\circ\text{C}) = 1.97 \cdot 10^{-16} \text{ m}^2/\text{s}$	$w_\eta^{Sn} = 0.59$
$\rho_{Sn} = 7.29 \cdot 10^3 \text{ kg/m}^3$		

Table 5.3 Values of densities, growth rate parameters and weight fractions of Sn in η and ε phases.

In the present work the initial heat treatment step was at 210°C . Hence, the values of k_η , and k_ε at 210°C from Barzi et al.[60] (Table 5.3) were used to obtain the expression for R_{Sn} , R_η and R_ε (in meters):

$$R_{Sn} = -1.378 \times 10^{-8} \times \sqrt{t} + \sqrt{R_o^2 - 0.964 \times 10^{-16} \times t} \quad (5.15)$$

$$R_\eta = 0.0273 \times 10^{-8} \times \sqrt{t} + \sqrt{R_o^2 - 0.964 \times 10^{-16} \times t} \quad (5.16)$$

$$R_\varepsilon = 0.882 \times 10^{-8} \times \sqrt{t} + \sqrt{R_o^2 - 0.964 \times 10^{-16} \times t} \quad (5.17)$$

For the second step of the heat treatment the assumption of a negligible Sn level in α phase is no longer valid. Thus, a different approach was used to obtain a relationship between the radii of these phases. The total moles of Sn leaving the Sn core in a time dt were equated to the total moles of Sn entering into the Sn/ η interface. Mathematically this is expressed as follows:

$$-\rho_{Sn} \cdot \frac{dV_{Sn}}{dt} = 2\pi R_{Sn} \cdot J \quad (5.18)$$

Where V_{Sn} (m²) is the volume per unit length of the Sn core at time t (s); J (kg/m²s) is the flux at the Sn/ η interface; R_{Sn} (m) is the instantaneous radius of Sn core; ρ_{Sn} (kg/m³) is the density of the pure-Sn.

According to the Fick's first law the flux of Sn atoms at the Sn/ η can be written as:

$$J = -\tilde{D}_{\eta} \frac{\partial c_{\eta}}{\partial y} \quad (5.19)$$

Where \tilde{D}_{η} (m²/s) is the interdiffusion coefficient in the η phase and $\partial c_{\eta}/\partial y$ is the concentration gradient in the direction of growth. Under the assumption of constant concentration at the boundaries of the η layer the concentration gradient $\partial c_{\eta}/\partial y$ in Equation 5.19 can be replaced by $\Delta c_{\eta}/y_{\eta}$, where Δc_{η} (kg/m³) is the concentration difference across the η phase and y_{η} (m) is the layer thickness of the η phase. After this substitution, the flux can be written as:

$$J \approx \tilde{D}_{\eta} \frac{\Delta c_{\eta}}{y_{\eta}} \quad (5.20)$$

Using the parabolic growth law for the growth of η phase, the layer thickness of the η phase at time t (y_{η}) can be written as

$$y_{\eta}^2 - y_{\eta_0}^2 = k_{\eta}(T) \cdot t \quad (5.21)$$

$$\therefore y_{\eta} = \sqrt{k_{\eta}(T) \cdot t + y_{\eta_0}^2} \quad (5.22)$$

Where y_{η_0} is the layer thickness of the η phase at time $t = 0$, i.e. the start of the second step of the heat treatment.

By combining equations (5.18), (5.20) and (5.22) and replacing V_{Sn} by πR_{Sn}^2 (i.e. the volume of Sn core per unit length of the wire), the following expression is obtained:

$$-\rho_{Sn} \frac{d[\pi R_{Sn}^2]}{dt} = 2\pi R_{Sn} \cdot [\tilde{D}_\eta \frac{\Delta c_\eta}{\sqrt{k_\eta(T) \cdot t + y_{\eta_0}^2}}] \quad (5.23)$$

Simplifying the above expression gives:

$$dR_{Sn} = -\frac{\tilde{D}_\eta \Delta c_\eta}{\rho_{Sn}} \frac{dt}{\sqrt{k_\eta(T) \cdot t + y_{\eta_0}^2}} \quad (5.24)$$

This upon integration gives:

$$R_{Sn}(t) = R_{Sn_0} - \frac{\tilde{D}_\eta \Delta c_\eta}{\rho_{Sn}} \times \frac{2(\sqrt{k_\eta \cdot t + y_{\eta_0}^2} - y_{\eta_0})}{k_\eta} \quad (5.25)$$

The above expression determines the radial position of Sn core as a function of temperature and time. Using this along with the parabolic growth expression for the η and ε phases, the expression for the radial positions of η and ε phases are obtained:

$$R_\eta = R_{Sn} + \sqrt{k_\eta \cdot t + y_{\eta_0}^2} \quad (5.26)$$

$$R_\varepsilon = R_\eta + \sqrt{k_\varepsilon \cdot t + y_{\varepsilon_0}^2} \quad (5.27)$$

Where y_{η_0} and y_{ε_0} are the thicknesses of η and ε phases at time $t = 0$. Thus, the expression obtained for the radial positions of Sn core, η and ε phases (Equations 5.25,

5.26, and 5.27 respectively) can be used to predict the radial positions of the three phases as a function of time and temperature. In the following section, the predicted radial positions of Sn-core, η and ε phases are compared with the experimentally observed values to verify the model.

5.5.2. Experimental Verification

Samples EG23, EG24 and GL28 (details are discussed in Section 3.1.1) were used to compare the predicted values of the radial positions of the phases with the experimentally observed values. The temperatures of the heat treatment for the first and second steps were 210°C and 400°C. The samples were heat treated for various times at these temperatures (Table 5.1). The radial positions of these phases were then measured from the SEM-BSE images using an image analysis software package (Section 4.2). These measured positions were then normalized to the outer radius of the subelements and plotted as a function of time (symbols in Figures 5.6 to 5.8). The predicted values calculated using the model (Equations 5.15 to 5.17 and 5.25 to 5.27) were then superimposed on these plots (curves in Figures 5.5 to 5.7).

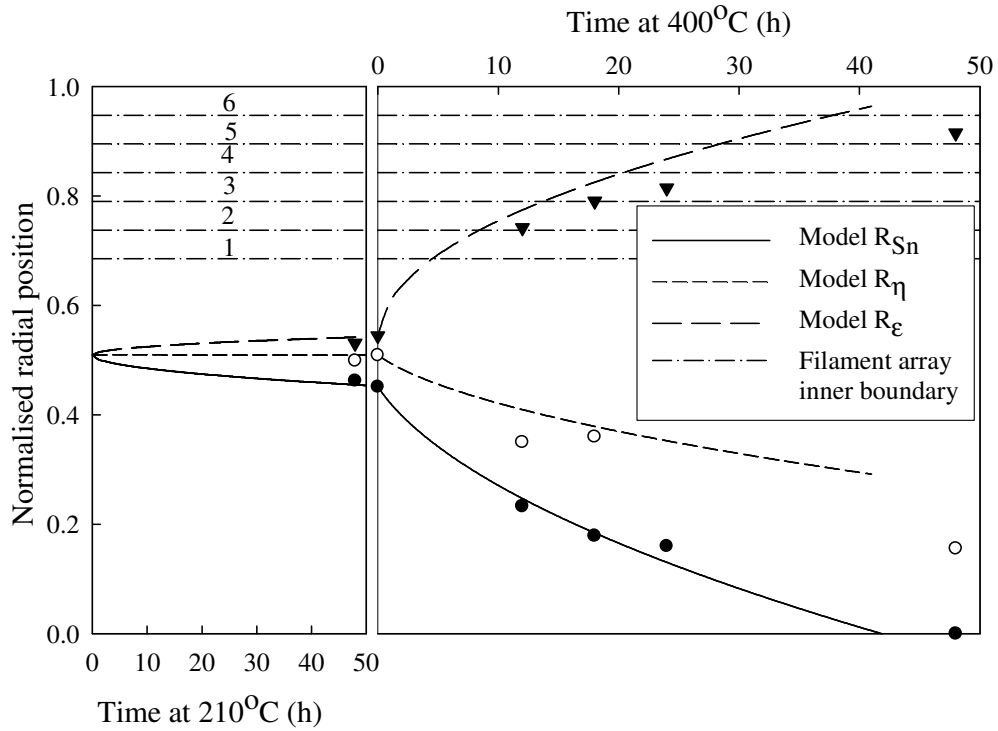


Figure 5.6 Radial positions within the subelement of η (○) and ϵ (▼) and pure Sn (●) phase for EG23 during pre-reaction heat treatment. Calculated curves for R_{η} (---), R_{ϵ} (—) and R_{Sn} (—) also shown. Horizontal dash-dot lines show inner boundaries of successive filamentary rows, six rows total. All radii normalized to R_{sub} .

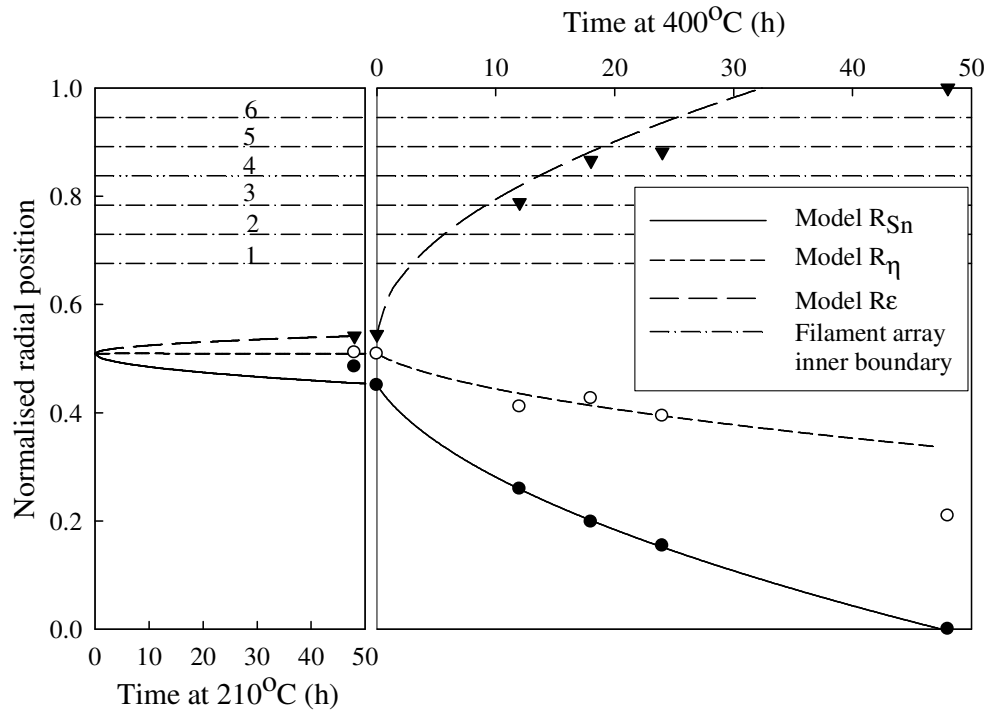


Figure 5.7 Radial positions within the subelement of η (\circ) and ϵ (\blacktriangledown) and pure Sn (\bullet) phase for EG24 during pre-reaction heat treatment. Calculated curves for R_{η} (---), R_{ϵ} (—) and R_{Sn} (—) also shown. Horizontal dash-dot lines show inner boundaries of successive filamentary rows, six rows total. All radii normalized to R_{sub} .

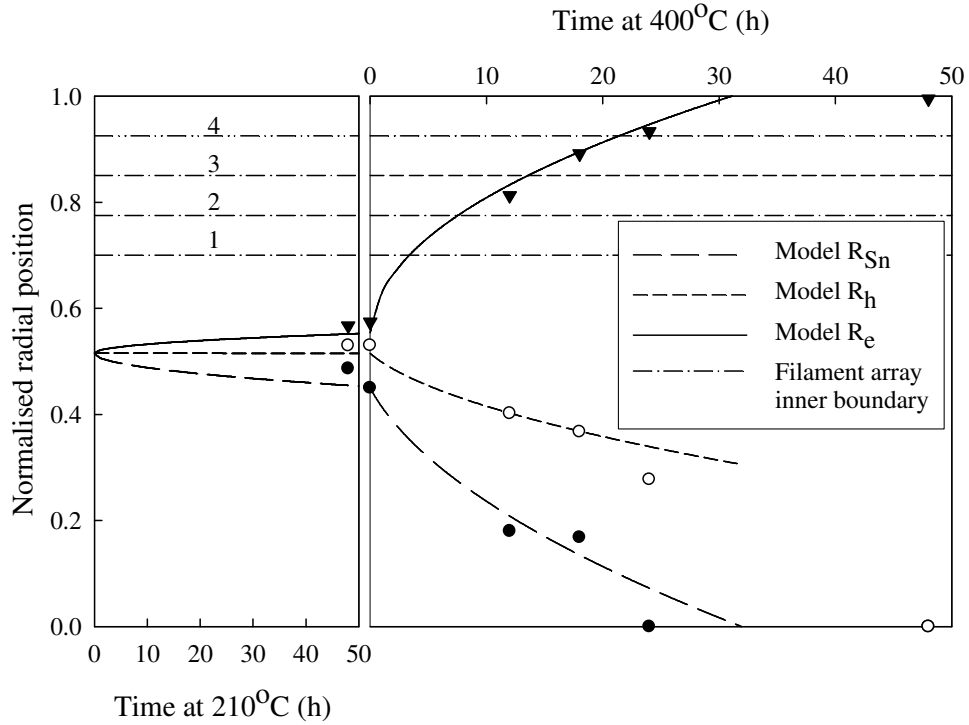


Figure 5.8 Radial positions within the subelement of η (\circ) and ε (\blacktriangledown) and pure Sn (\bullet) phase for GL28 during pre-reaction heat treatment. Calculated curves for R_η (---), R_ε (—) and R_{Sn} (— · —) also shown. Horizontal dash-dot lines show inner boundaries of successive filamentary rows, six rows total. All radii normalized to R_{sub} .

Figures 5.6 to 5.8 showing a reasonable agreement between the calculated radial positions of the phases using the model and the experimentally measured values. Hence, the model's prediction can be used to design the pre-reaction heat treatment parameters for subelements.

5.6 Growth Rates of Nb_3Sn Formation

Four types of superconducting strands (subelements-G0, G2, G3 and G4) described in section 3.1.2, were heat treated for various times at three different temperatures (675°C, 700°C, and 725°C). The details of the heat treatment schedule are given in Table 5.4. The cross-section of each of the strands was examined using SEM after heat treatment to

investigate the growth process of the Nb₃Sn phase. Figure 5.9 shows the SEM-BSE images of the cross-section of G2 after heat treatment at 675°C for various times (i.e. 0 h, 10 h, 24 h, 80 h, 150 h and 225 h). After 10 hours at 675°C, the Nb filaments and the barrier were partially converted into Nb₃Sn. The Nb filaments were fully converted to Nb₃Sn after 24 hours whereas the barrier was still only partially reacted. After 150 hours the Nb₃Sn layer reaches up to the boundary of the barrier and further heat treatment leads to the diffusion of Sn into the outer Cu matrix.

Steps (ramp rate)	Step I (10°C/h)	Step II (25°C/h)	Step III (50°C/h)
HT-1	210°C/48h	400°C/100h	675°C/ 0, 5, 10, 24, 40, 80, 100, 150, 200, 225 h
HT-2	210°C/48h	400°C/100h	700°C/ 0, 5, 10, 24, 40, 80, 100, 150, 200, 225 h
HT-3	210°C/48h	400°C/100h	725°C/ 0, 5, 10, 24, 40, 80, 100, 150, 200, 225 h

Table 5.4 Heat treatment schedule for four different types of subelement G0, G2, G3 and G4.

In order to compare the growth of the Nb₃Sn layer at three different temperature levels in the four types of subelement, the thickness of the Nb₃Sn layer in the barrier was measured. The layer thickness for each of the strand as a function of temperature and time is shown in Figure 5.10. It can be observed that the layer growth rate increases as the temperature of heat treatment increases from 675°C to 725°C. Also the strand with no Ti addition (G0) has a lower growth rate as compared to the strands with Ti addition (G2,

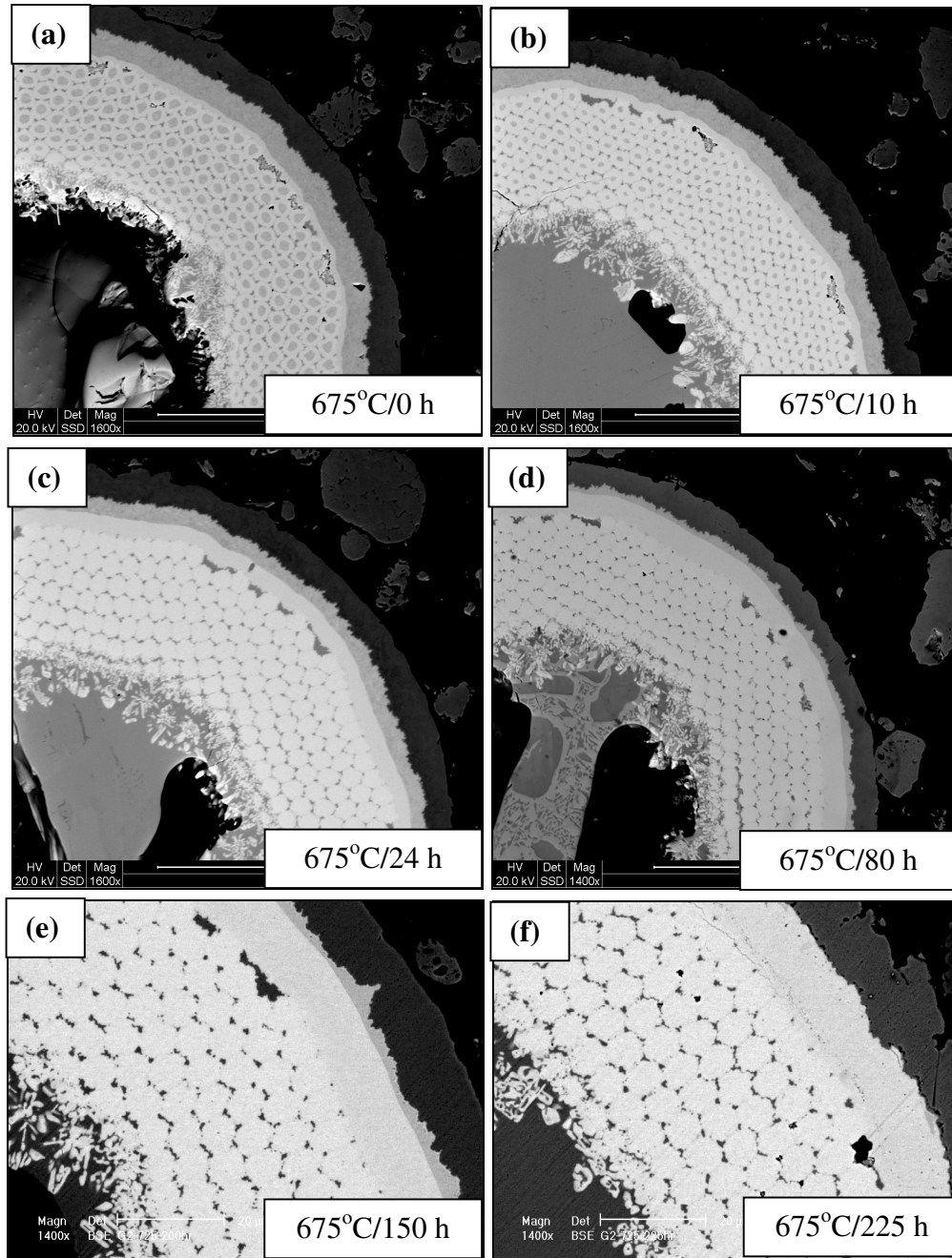


Figure 5.9. Cross-sections of subelement G2 after heat treatment at 675°C for various times; (a) and (b) show that the Nb filaments and the Nb barrier are not fully converted into Nb₃Sn phase; (c) and (d) show that all the Nb filaments are converted into Nb₃Sn while the some portion of the Nb barrier is still unreacted; (e) and (f) Both the filaments and the barrier are converted to Nb₃Sn phase. In (f) the Sn has leaked into the outer Cu-matrix as the heat treatment time was too long (i.e. 225 h).

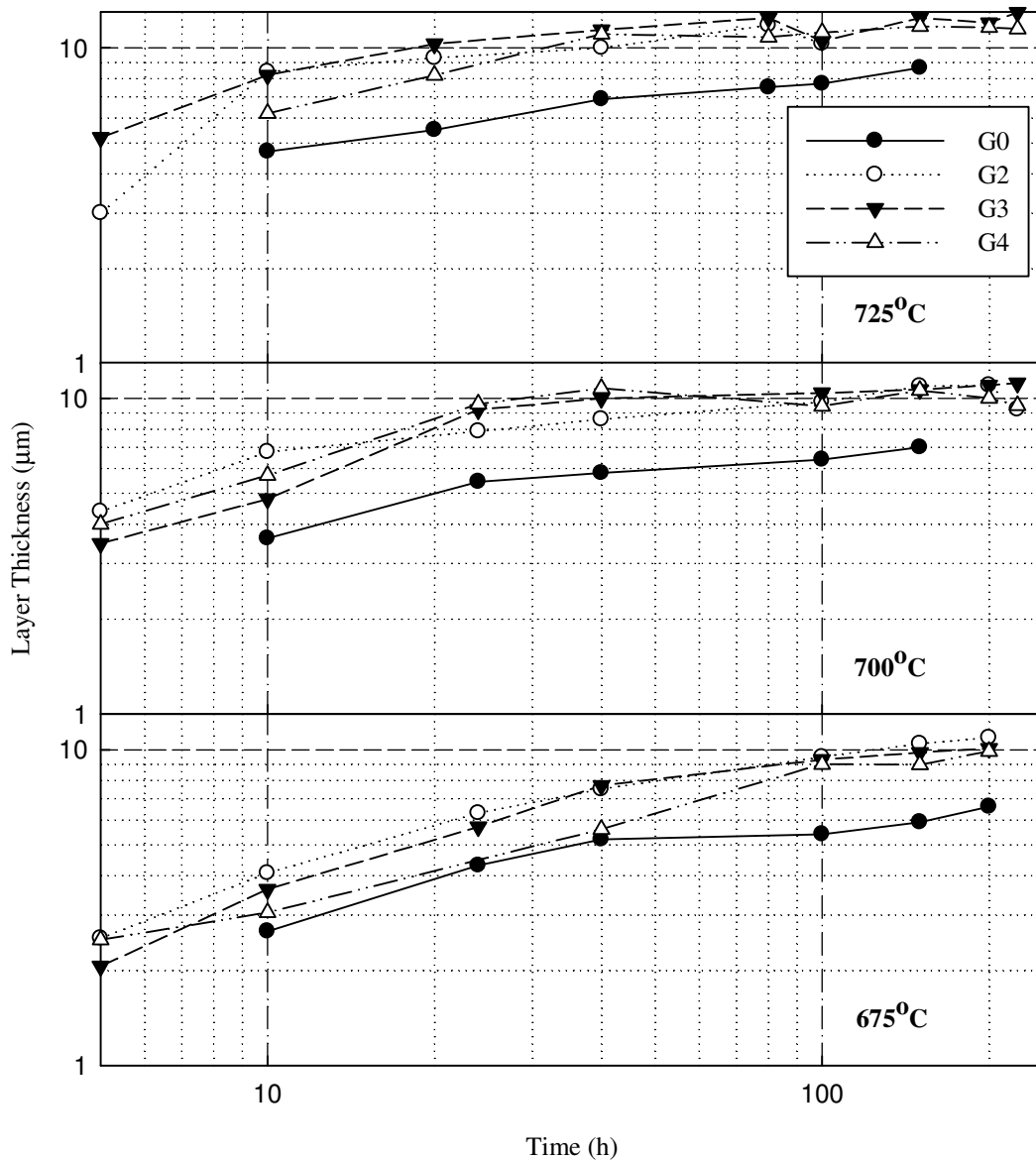


Figure 5.10 Nb₃Sn layer growth in the barrier for each subelement type as a function of heat treatment time at three different temperature levels (675°C, 700°C, and 725°C).

G2, G3 and G4). In order to have an approximate estimate of the growth rate, Equation 5.8 was fitted to the layer growth data. Considering the strand geometry, size, limited availability of Sn to diffuse, and the large compositional range of the Nb₃Sn intermetallic compound, a deviation in the value of the exponent n from 2 is expected [55].

The growth rate parameters determined by fitting the Equation 5.8 are presented in Table 5.5. Only the early stage (up to 40 hr) data were used to avoid the effect of Sn depletion at longer times. The values of the exponent n are higher in G0 as compared to that of the other strands. The rate of growth is faster in the strands having Ti addition (G2, G3, and G4). Similar effect of Ti on Nb₃Sn layer growth was also observed by Wu *et al.* [61]. These extracted values are useful to estimate and compare the layer growth for the different levels of Ti doping at various temperature. The layer growth parameters determined by S. Mattafirri [59] for internal-Sn (IT) strands are also shown in Table 5.5.

T (°C)	G0		G2		G3		G4	
	k (m ⁿ /s)	n	k (m ⁿ /s)	n	k (m ⁿ /s)	n	k (m ⁿ /s)	n
675°C	$1.2 \cdot 10^{-16}$	2.0	$1.2 \cdot 10^{-14}$	1.7	$2.6 \cdot 10^{-15}$	1.84	$4.3 \cdot 10^{-17}$	2.1
700°C	$8.5 \cdot 10^{-16}$	2.1	$1.6 \cdot 10^{-13}$	1.6	$9.9 \cdot 10^{-14}$	1.60	$1.2 \cdot 10^{-14}$	1.8
725°C	-	-	$4.7 \cdot 10^{-15}$	1.9	$1.1 \cdot 10^{-15}$	2.02	$9.6 \cdot 10^{-18}$	2.4
From S. Mattafirri [59] $k = 5.45 \cdot 10^{-14}$ m ⁿ /s and $n = 1.46$ for IT strands at 700°C								

Table 5.5 k and n for Nb₃Sn layer growth in the barrier of G0-G4 subelements.

CHAPTER 6

EFFECTS OF Ti ADDITIONS ON THE SUPERCONDUCTING PROPERTIES

6.1 Introduction

To study the effect of Ti additions, the superconducting properties of strands having various levels of Ti (ranging from 0 to 2.8 at %) were evaluated after various heat treatments. In the following section the upper critical field (B_{c2}) and critical current density (J_c) values of these strands are presented. The sample specifications are presented in Section 3.1.2.

The B_{c2} measurements were carried out at National High Magnetic Field Laboratory (NHMFL). The method of measurement is described in Section 4.5. The J_c measurements were done for some selected sample in the magnetic field range of 10 T to 33 T. The J_c (A/mm^2) is defined as critical current capacity I_c (A) per unit cross-sectional area of the strand. In this study the area under the barrier was considered to calculate the J_c from the I_c values. The J_c measurement method is illustrated in Section 4.3.

SEM-EDS measurements were also performed on the Nb_3Sn phase to investigate the Sn and Ti composition and their correlation with the measured properties (B_{c2} and J_c) of these strands.

6.2 Effect of Ti addition on B_{c2} Values

Table 6.1 shows the B_{c2} values for the four strands (G0, G2, G3 and G4) heat treated at three different temperatures (675°C, 700°C and 725°C) for heat treatment durations varying from 100 hrs to 225 hrs. The optimum value of B_{c2} at each temperature for each of the strands is shown in bold text in the table. The maximum value of B_{c2} , 28.91 T, was observed in strand G0 heat treated at 700°C for 150 hrs. In order to identify the pattern in B_{c2} values for these strands, the optimum values at each temperature level for each of the strands were plotted in Figure 6.1.

B_{c2} initially increases with increasing heat treatment temperature due to the increasing Sn level in the A15. The B_{c2} value is maximum at 700°C for all strands except G3 which has maximum B_{c2} value at a heat treatment of 675°C/200 h. The values for all strands drop as the temperature is increased to 725°C, which was not initially expected, but in retrospect seems to be due to depleting the Sn-source, and Sn diffusion through a fully reacted barrier leading to a drop in A15 stoichiometry. It can be noted that at least for the present samples and heat treatments, Ti additions in presence of Ta have not improved the B_{c2} .

	675°C				700°C				725°C			
	100 hr	150 hr	200 hr	225 hr	100 hr	150 hr	200 hr	225 hr	100 hr	150 hr	200 hr	225 hr
G0	27.03	27.35	28.68	-	26.71	28.91	-	-	26.96	27.50	-	-
G2	27.48	26.92	25.99	-	28.77	26.85	27.07	-	28.11	27.52	26.00	-
G3	27.52	27.85	27.79	-	27.8	26.70	26.80	27.07	27.15	27.39	27.03	27.19
G4	27.20	27.04	27.25	-	27.50	27.79	27.06	27.92	27.6	-	27.60	27.13

Table 6.1 B_{c2} values (in Tesla) for the four strand types (G0, G2, G3, and G4) after heat treatment at three different temperatures (675°C, 700°C and 725°C) for heat treatment durations ranging from 100 hours to 225 hours. The optimum value of B_{c2} at each temperature for each of the strands is shown as bold.

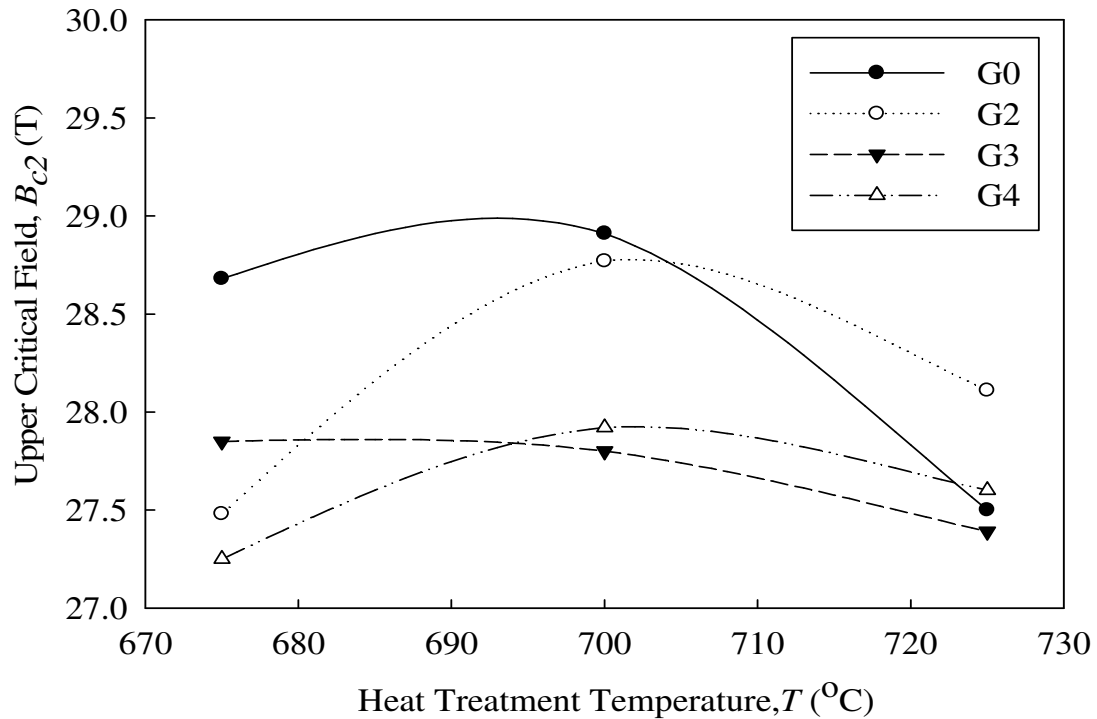


Figure 6.1 Maximum B_{c2} as a function of temperature for all the four strand types. The maximum B_{c2} (resistive measurement) was selected (shown as bold text in Table 6.1) from the five different heat treatment durations (100 h, 150 h, 200, 200 h, and 225 h).

6.3 Effect of Ti addition on J_c Values

Figure 6.2 shows the J_c values measured for the strands which had the highest B_{c2} values in each strand category. Values of 3400 A/mm^2 and 3100 A/mm^2 at 12 T were achieved in G0 and G3 strands heat treated at $700^\circ\text{C}/150 \text{ h}$ and $675^\circ\text{C}/200 \text{ h}$ respectively. The J_c values for G2 and G4 at 12 T are approximately 2500 A/mm^2 . The decrease in J_c for G4 as compared to G0 and G3 could be due to the leakage of Sn in the matrix as the heat treatment for this wire was too long (225 h at 700°C).

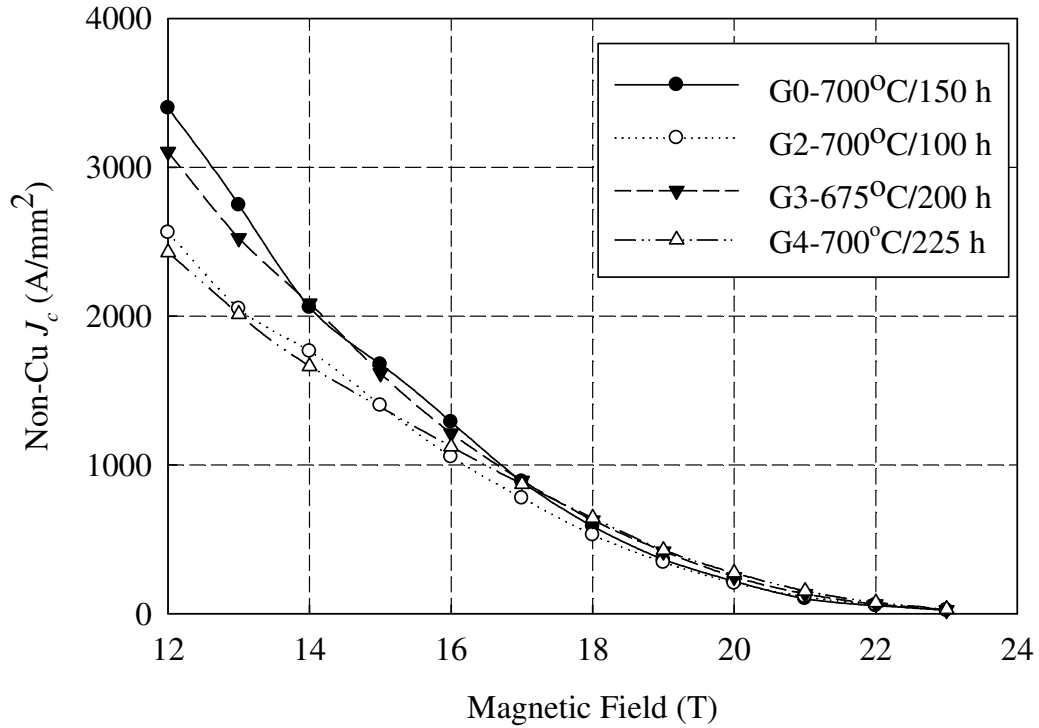


Figure 6.2 Non-Cu J_c values of strands having the optimum critical field (B_{c2}) for each strand type.

6.4 Discussion

In addition to the resistive measurements of the B_{c2} , the values of B_{c2} were also determined by Kramer plot (the plot of $J_c^{1/2}B^{1/4}$ as function of magnetic field at constant temperature results in linear dependencies) [62]. The Kramer plot is shown in the Figure 6.3. The Kramer plot extracted values of B_{c2} along with the resistively measured values are listed in the Table 6.2. The B_{c2} values based on Kramer extrapolations are lower than the resistively measured values and have a trend different from that of the resistively measured values. The Kramer- B_{c2} values increase from 23.1 T to 24.4 T as the Ti level increases whereas the resistively measured B_{c2} values decrease from 28.9 T to 27.9 T as

the Ti level increases. To explain these results the actual Sn and Ti compositions in the Nb_3Sn phase were determined using SEM-EDS. Figure 6.4 shows the Sn compositional profile across the Nb_3Sn filaments. The average compositions of Sn and Ti in the Nb_3Sn phase for each strand are also shown in Table 6.2. Note that the 0-2.8at% Ti in the Sn core was designed to give 0-0.63% Ti in the final A15 Nb_3Sn phase, and the results are close to this. G0 has the largest variation in Sn composition across the sample. The Kramer-extracted B_{c2} are suppressed by this variation. The resistively measured B_{c2} values are still quite high, because the resistive measurements probe the best part of the sample assuming parallel-path connections of regions with differing stoichiometry [25]. The strand G2 and G3 have less Sn variation, and show more agreement between Kramer and resistively measured results. Strand G4 has a relatively high Sn content, as well as a low Sn gradient. In fact, it is near the region where we might expect a tetragonal transformation at lower temperatures. This may explain the slightly lower B_{c2} values (assuming Ti is not suppressing cubic to tetragonal transformation), or it may be that Ti is over doped.

Strand	HT	Ti (Design at %)	Ti (at% ave)	Sn (at% ave)	12 T J_c (A/mm ²)	B_{c2} Values (T)	
						Kramer extrapolated	Resistively Measured
G0	700°C /150h	0	0	22.9	3397	23.1	28.9
G2	700°C /100h	0.35	0.26	23.2	2559	23.6	28.8
G3	675°C /200h	0.53	0.44	23.5	3102	23.7	27.9
G4	700°C /225h	0.70	0.63	24.1	2427	24.4	27.9

Table 6.2 Comparison of J_c and B_{c2} values for the strands with their heat treatment optimized for B_{c2} .

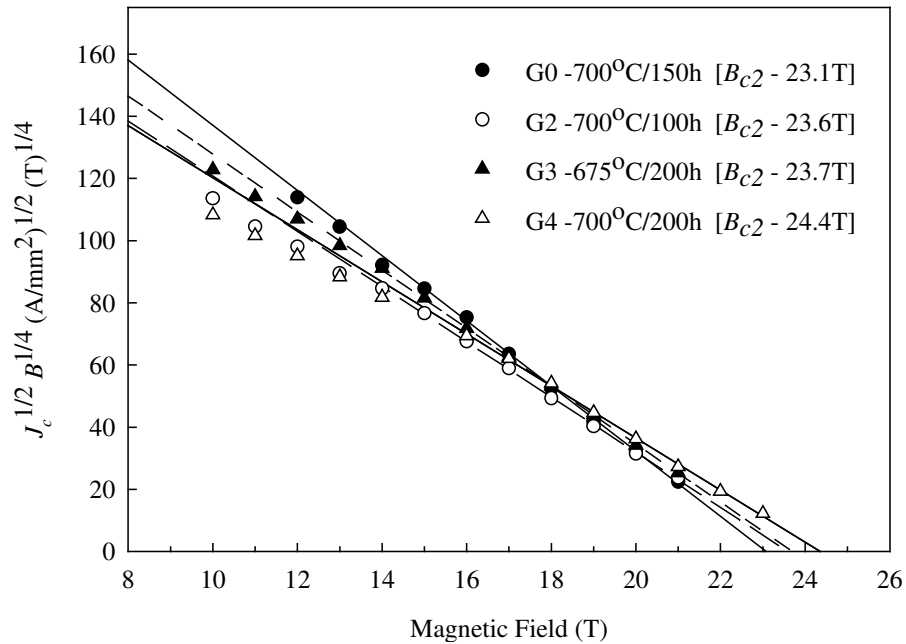


Figure 6.3 Kramer plots for the strands with maximum B_{c2} . Values determined from the plot are shown in the legend. Kramer plot was fit to 16-23 T data only.

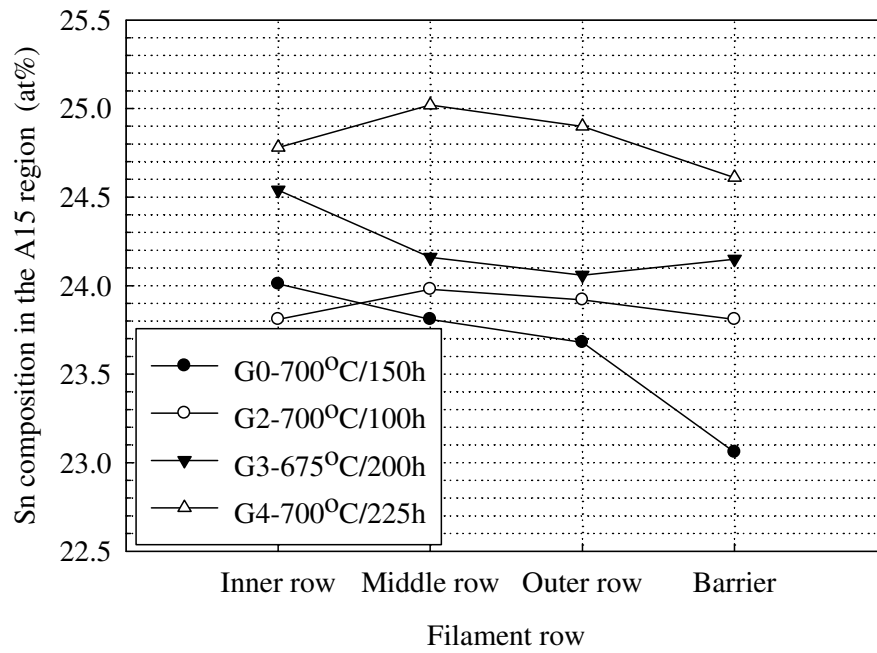


Figure 6.4 Sn composition in the reacted A15 region for strands which have maximum B_{c2} value (for each strand type). The EDS spot was at the center of the filaments.

CHAPTER 7

CONCLUSION

A series of pre-reaction heat treatments were performed on Internal-Tin type superconducting strands to understand the formation of various Cu-Sn intermetallic phases during the heat treatment process. The layer growths of η and ε phases were investigated experimentally and theoretically. Growth rate constants were obtained for η and ε phases at 400°C. These were in general agreement with those in the literature, and did not appear to be strongly influenced by the presence of Ta or Ti, but seem to be affected to a small degree by Nb/Sn fraction. A simple analytical model was demonstrated which can be used to predict the radial positions of Sn, η and ε phases in the pre-reaction phase of the heat treatment.

Following the pre-reaction heat treatment studies, the effects of Ti doping in the presence of Ta on the kinetics of Nb₃Sn formation and superconducting properties of internal-tin type strands were investigated. It was seen that the Ti additions to the Sn source tend to speed up the kinetics of formation of Nb₃Sn. The growth rate was faster in strands having Ti as compared to the strand with no Ti. The non-Cu J_c at 14 T was almost the same in the Ta doped ternary Nb₃Sn (G0) and in the quaternary doped Nb₃Sn (G3). The maximum value of B_{c2} of 28.9 T was seen in strand (G0) having ~3.5 at% Ta with

~24 at% Sn in the A15 phase. The strand with an addition of 1.4 at% Ti in the core has slightly higher Sn content and almost similar B_{c2} as compared to the unalloyed core strand. Further addition of Ti (up to 2.8 at %) decreased the B_{c2} value by approximately 1 T. Transport measurements for present samples were slightly higher with Ti additions above 18 T. It was also interesting to note that at very long heat treatment times at elevated temperatures, Sn content and the associated critical field parameters could be decreased, apparently by diffusion from the A15 to the bronze, if a Sn-sink in the form of diffusion through a reacted barrier was present. In summary, at least for our present samples and heat treatments, Ti additions in presence of Ta have not improved the B_{c2} , although excellent subelement properties were seen. These results suggest that the 7.5 wt% Ta doping in Nb is an optimal level and further addition of Ti to it increases the resistivity to an extent where the B_{c2} starts decreasing.

LIST OF REFERENCES

- [1] K. Tachikawa, Y. Ikeda, Y. Koyata, H. Izawa, and T. Takeuchi, "Structure and high-field performance of (Nb,Ta)₃Sn superconducting wires prepared from Sn-Ta sheets," *Journal of the Japan Institute of Metals*, vol. 68, pp. 624-628, 2004.
- [2] P. J. Lee, C. M. Fischer, M. T. Naus, M. C. Jewell, A. A. Squitieri, and D. C. Larbalestier, "The microstructure and micro-chemistry of high critical current Nb₃Sn strands manufactured by the Bronze, Internal-Sn and PIT techniques," *IEEE Transactions on Applied Superconductivity*, vol. 13, pp. 3422-3425, 2003.
- [3] S. Foner, R. Roberge, E. J. M. Jr., B. B. Schwartz, and J. L. Fihey, "Mechanical properties of in situ multifilamentary niobium-tin (Nb₃Sn) superconducting wires," *Applied Phys. Lett.*, vol. 34, pp. 241-243, 1979.
- [4] M. F. Sykes and J. W. Essan, "Critical percolation probabilities by series methods," *Phys. Rev.*, vol. 133, pp. A310-A315, 1964.
- [5] R. Roberge, S. Foner, E. J. M. Jr., B. B. Schwartz, and J. L. Fihey, "Effects of stress and strain on the critical current density of "in situ" multifilamentary superconducting wires in high magnetic fields," *IEEE Transactions on Magnetics*, vol. MAG-15, pp. 687-688, 1979.
- [6] J. L. Fihey, R. Roberge, S. Foner, E. J. M. Jr., and B. B. Schwartz, "Multifilamentary vanadium-gallium (V₃Ga) produced by the in situ process," *Advances in Cryogenic Engineering*, vol. 26, pp. 350-357, 1980.
- [7] A. Nagata, H. Hirayama, K. Noto, and O. Izumi, "Superconducting properties and microstructure in dilute alloy containing small amounts of V₃Ga particles " *Journal of Applied Physics*, vol. 48, pp. 5175-5179, 1977.

- [8] S. Kirkpatrick, "Classical transport in disordered media: scaling and effective-medium theories," *Phys. Rev. Lett.*, vol. 27, pp. 1722-1725, 1971.
- [9] T. Luhman and M. Suenaga, "The influence of thermally induced matrix stresses on the superconducting properties of niobium-tin (Nb_3Sn) wire conductors," *IEEE Transactions on Magnetics*, vol. MAG-13, pp. 800-802, 1977.
- [10] H. Hillmann, H. Kuckuck, E. Springer, H. J. Weisse, M. Wilhelm, and K. Wohlleben, "Coil performance of multifilamentary niobium-tin (Nb_3Sn) conductors," *IEEE Transactions on Magnetics*, vol. MAG-15, pp. 205-208, 1979.
- [11] P. E. Johnson-Walls, D. R. Dieterich, W. V. Hassenzahl, and J. W. Morris, "The microstructural state of Nb_3Sn in a multifilamentary titanium doped bronze-process wire," *IEEE Transactions on Magnetics*, vol. 21, pp. 1137-1139, 1985.
- [12] K. Kamata, N. Tada, K. Itoh, and K. Tachikawa, "Optimization of critical currents in composite-processed multifilamentary niobium-tin (Nb_3Sn) conductors with niobium-titanium alloy cores," *IEEE Transactions on Magnetics*, vol. 19, pp. 1433-1436, 1983.
- [13] M. Suenaga, C. J. Klamut, and W. K. McDonald, "Superconducting critical current densities of pure and alloyed (Ti) Nb_3Sn multifilamentary wires by the expanded-metal process," *IEEE Transactions on Magnetism*, vol. 19, pp. 1425-1428, 1983.
- [14] K. Tachikawa, T. Asano, and T. Takeuchi, "High-field superconducting properties of the composite-processed Nb_3Sn with Nb-Ti alloy cores," *Applied Phys. Lett.*, vol. 39, pp. 766-768, 1981.
- [15] N. J. Pugh, J. E. Evetts, and E. R. Wallach, "A transmission electron microscopy study of bronze-processed Nb_3Sn and $(\text{Nb}, \text{Ta})_3\text{Sn}$ multifilamentary superconducting wire," *Journal of Materials Science*, vol. 20, pp. 4521-4526, 1985.
- [16] N. J. Pugh, J. L. M. Robertson, E. R. Wallach, J. R. Cave, R. E. Somekh, and J. E. Evetts, "Microstructure development in bronze route Nb_3Sn and $(\text{Nb}, \text{Ta})_3\text{Sn}$ multifilamentary composites," *IEEE Transactions on Magnetics*, vol. 21, pp. 1129-1132, 1985.

- [17] M. Suenaga, *Superconductor Materials Science-Metallurgy, Fabrication and Applications*. New York and London: Plenum Press, 1980.
- [18] M. T. Naus, "Optimization of Internal-Sn Nb₃Sn Composites," PhD Thesis, University of Wisconsin-Madison, 2002.
- [19] H. K. Onnes, *Leiden Communication*, vol. 120, 1911.
- [20] W. Meissner and R. Ochsenfeld, "Ein neuer Effect bei Eintritt der Supraleitfähigkeit," *Naturwissenschaften*, vol. 21, p. 787, 1933.
- [21] J. Bardeen, L. N. Cooper, and J. R. Schrieffer, "Theory of Superconductivity," *Phys. Rev.*, vol. 108, p. 1175, 1957.
- [22] T. P. Orlando, J. E. J. McNiff, S. Foner, and M. R. Beasley, "Critical fields, Pauli paramagnetic limiting, and material parameters of Nb₃Sn and V₃Si " *Phys. Rev. B*, vol. 19, p. 4545, 1979.
- [23] R. M. Scalapin, "Superconducting materials," *Annual Review Materials Science*, pp. 10:113-132, 1980.
- [24] R. W. Cahn and P. Haasen, *Physical Metallurgy*, Fourth ed. vol. 2, 1996.
- [25] A. Godeke, "Performance Boundaries in Nb₃Sn Superconductors," PhD. Thesis, University of Twente, 2005.
- [26] H. Devantay, J. L. Jorda, M. Decroux, J. Muller, and R. Flukiger, "The physical and structural properties of superconducting A15-type Nb-Sn alloys," *Journal of Materials Science*, vol. 16, p. 2145, 1981.
- [27] J. P. Charlesworth, I. MacPhail, and P. E. Madsen, "Experimental work on the niobium-tin constitution diagram and related studies," *Journal of Materials Science*, vol. 5, p. 580, 1970.
- [28] R. Mailfert, B. W. Batterman, and J. J. Hanak, "Low-temperature structural transformation in Nb₃Sn," *Phys. Lett.*, vol. 24, p. 315, 1967.

- [29] R. Flukiger, W. Schauer, and W. Goldacker, "Superconductivity in d- and f-Band Metals," *Kernforschungszentrum Karlsruhe*, pp. 41-44, 1982.
- [30] J. J. Hanak, K. Strater, and G. W. Cullen, "Preparation and properties of vapor-deposited niobium stannide," *RCA (Radio Corporation of America) Review (U.S.)*, vol. 25, p. 342, 1964.
- [31] J. D. Livingston, "Effect of tantalum additions to bronze-processed niobium-tin (Nb_3Sn) superconductors," *IEEE Transactions on Magnetics*, vol. MAG-14(5), p. 611, 1978.
- [32] S. Miyashita, K. Yoshizaki, K. Hashimoto, and K. Tachikawa, "Effects of titanium addition to the Nb_3Sn wires fabricated by the internal tin diffusion process," *IEEE Transactions on Magnetics*, vol. MAG-23, pp. 629-632, 1987.
- [33] M. Suenaga, C. J. Klamut, N. Higuchi, and T. Kuroda, " Properties of Ti alloyed multifilamentary Nb_3Sn wires by internal tin process," *IEEE Transactions on Magnetics*, vol. 21, pp. 305-308, 1985.
- [34] M. Suenaga, K. Tsuchiya, and N. Higuchi, "Superconducting critical current density of bronze processed pure and alloyed Nb_3Sn at very high magnetic fields (up to 24 T)," *Applied Phys. Lett.*, vol. 44, p. 919, 1984.
- [35] M. Suenaga, D. O. Welch, R. L. Sabatini, O. F. Kammerer, and S. Okuda, "Superconducting critical temperatures, critical magnetic fields, lattice parameters, and chemical compositions of bulk pure and alloyed Nb_3Sn produced by the bronze process," *Journal of Applied Physics*, vol. 59, p. 840, 1986.
- [36] K. Tachikawa, H. Sekine, and Y. Iijima, "Composite-processed Nb_3Sn with titanium addition to the matrix," *Journal of Applied Physics*, vol. 53, p. 5354, 1982.
- [37] R. Flukiger, *Atomic Ordering, Phase Stability and Superconductivity in Bulk and Filamentary A15 Type Compounds*, 1987.
- [38] Y. B. Kim, C. F. Hempstead, and A. R. Strnad, "Flux-flow Resistance in Type II Superconductors," *Phys. Rev.*, vol. 139, p. A1163, 1965.

- [39] T. Pyon and E. Gregory, "Some effects of matrix additions to internal tin processed multifilamentary Nb₃Sn superconductors," *IEEE Transactions on Applied Superconductivity*, vol. 5, p. 1760, 1995.
- [40] V. Abacherli, F. Buta, D. Uglietti, C. Senatore, B. Seeber, and R. Flukiger, "Investigation on the Effect of Ta addition on J_c and n of (Nb,Ti)₃Sn Bronze Processed Multifilamentary Wires at High Magnetic Fields," *IEEE Transactions on Applied Superconductivity*, vol. 17, pp. 2564-2567, 2007.
- [41] M. B. Field, J. A. Parell, Y. Zhang, and S. Hong, "Nb₃Sn conductor development for fusion and particle accelerator applications," *Advances in Cryogenic Engineering*, vol. 52, pp. 544-549, 2006.
- [42] E. Gregory, M. Tomsic, M. D. Sumption, X. Peng, X. Wu, E. W. Collings, and B. A. Zeitlin, "The introduction of titanium into internal-tin Nb₃Sn by a variety of procedures," *IEEE Transactions on Applied Superconductivity*, vol. 15, pp. 3478-3481, 2005.
- [43] J. A. Parell, M. B. Field, Y. Zhang, and S. Hong, "Advances in Nb₃Sn strand for fusion and particle accelerator applications," *IEEE Transactions on Applied Superconductivity*, vol. 15, pp. 1200-1204, 2005.
- [44] A. R. Kaufmann and J. J. Pickett, "Multifilament Nb₃Sn superconducting wire," *Bulletin American Physics Society*, vol. 15, p. 838, 1970.
- [45] A. Vorobieva, A. Shikov, A. Silaev, E. Dergunova, V. Lomaev, M. Nasibulin, K. Mareev, and S. Kuznetsov, "Study of Nb₃Sn with enhanced characteristics for ITER," *IEEE Transactions on Applied Superconductivity*, vol. 11, pp. 3588-3590, 2001.
- [46] M. Hansen, *Constitution of Binary Alloys*: McGraw Hill, 1958.
- [47] S. Foner and B. B. Schwartz, *Superconductor Material Science*. N.Y.: Plenum Press, 1981.
- [48] Y. Hashimoto, K. Yoshizaki, and M. Tanaka, in *Proceedings of 5th International Cryogenic Engineering Conference*, Kyoto, Japan, 1974, p. 332.

- [49] E. Barzi, G. Ambrosio, P. Bauer, J. M. Rey, R. Yamada, and A. Ziobin, "Progress Report on Strand and Cable R&D," Fermilab TD-01-013, 2001.
- [50] J. D. Elen, C. A. M. v. Beijnen, and C. A. M. v. d. Klein, "Multifilament V₃Ga and Nb₃Sn superconductors produced by the ECN-technique," *IEEE Transactions on Magnetism*, vol. MAG-13, p. 470, 1977.
- [51] G. M. Ozeryansky and E. Gregory, "A new internal-tin Nb₃Sn conductor made by a novel manufacturing process," *IEEE Transactions on Applied Superconductivity*, vol. 27, pp. 1755-1758, 1991.
- [52] S. B. Dove, "UTHSCSA Image Tool," <http://ddsdx.uthscsa.edu/dig/itdesc.html>, 2002.
- [53] R. E. Lee, *Scanning Electron Microscopy and X-ray Microanalysis*: P T R Prentice- Hal, Inc., 1993.
- [54] W. Goldacker, R. Ahrens, M. Nindel, B. Obst, and C. Meingast, "HIP synthesized Nb₃Sn bulk materials with extraordinary homogeneity," *IEEE Transactions on Applied Superconductivity*, vol. 3, pp. 1322-1325, 1993.
- [55] V. M. Falchenko, L. N. Larikov, and V. R. Ryabov, *Diffusion Processes in Solid-Phase Welding of Materials*. New Delhi: Oxonian Press, 1984.
- [56] J. H. Westerbook and R. L. Fleischer, *Intermetallic compounds-principles and practice* vol. 1: John Willey and Sons Ltd., 1995.
- [57] G. Tammann and J. J. Rocha, "The diffusion of two metals into one another with formation of intermetallic compounds," *Zeit. Fur. Anorg. Chemie.*, vol. 199, p. 289, 1931.
- [58] M. Wein, L. Levin, and S. Nadiv, "The mechanism of mixing and reactive diffusion in intermetallics (1:2 titanium-iron and 1:2 titanium-chromium compounds)," *Phil. Mag. A*, vol. 38, p. 81, 1978.
- [59] S. Mattafirri, "Kinetics of phase growth during Cu-Sn diffusion process and the Nb₃Sn formation, Optimization of superconducting properties.," M.S. Thesis, Universita Degli Studi Di Pisa, 2002.

- [60] S. Mattafirri, E. Barzi, F. Fineschi, and J.-M. Rey, "Kinetics of phase growth in the Cu-Sn system and application to composite Nb₃Sn strands," *IEEE Transactions on Applied Superconductivity*, vol. 13, June 2003 2003.

- [61] X. Wu, X. Peng, M. D. Sumption, M. Tomsic, E. Gregory, and E. W. Collings, "Ti and Sn diffusion and its influence on phase formation in internal-tin Nb₃Sn superconductor strands," *IEEE Transactions on Applied Superconductivity*, vol. 15, pp. 3399-3402, 2005.

- [62] E. J. Kramer, "Scaling laws for flux pinning in hard superconductors," *Journal of Applied Physics*, vol. 44, p. 1360, 1973.